MANIPULATING AND CHARACTERIZING NANOSCALE PARTICLES USING NEAR-FIELD OPTICAL FORCES

A Dissertation

Presented to the Faculty of the Graduate School

of Cornell University

in Partial Fulfillment of the Requirements for the Degree of

Doctor of Philosophy

by

Dakota O'Dell

January 2017

MANIPULATING AND CHARACTERIZING NANOSCALE PARTICLES USING NEAR-FIELD OPTICAL FORCES

Dakota O'Dell, Ph.D.

Cornell University 2017

In the three decades since the development of optical tweezers, optical trapping has become an invaluable technique for particle manipulation and is used widely in biology as well as material science. In more recent years, there has been a significant effort to integrate optical traps directly with microfluidics on-chip to produce stronger optical forces and manipulate even smaller particles. This is often achieved through the use of near-field forces produced by subwavelength optical confinement. By leveraging techniques and designs from photonics, near-field optics can generate very strong piconewton forces that act over nanometer length scales.

This dissertation aims to exploit these unique features of near-field optical forces– their strength, tunability, and precise localization– to build new nanostructures, develop new optical spectroscopy techniques, and probe the fundamental nature of particles and their interactions on the nanoscale. In the first half of this work, I focus on using optical gradient forces to drive the assembly of hybrid photonic-plasmonic resonators and using the amplified forces from these resonators to trap, manipulate, and bind other nanoparticles. These resonators are then used to optically drive the adsorption of individual proteins as a way of measuring the activation energy barrier of those adsorption reactions.

While colloidal nanoparticles are critical in a wide range of fields and industries, there is still no reliable theoretical framework to describe their behavior in realistic

solution conditions. This issue is compounded by the difficulty of directly measuring nanoscale particles with conventional optical tools. In the latter half of this work, I have demonstrated that near-field optical forces, which operate at similar magnitudes and length scales as colloidal forces, can be used to study the properties of nanoparticles directly. By applying a known optical force to a particle with an optical waveguide, the size and properties of the particle can be extracted from its dynamic response to that applied force. This technique leverages the unique advantages of localized optical forces and allows for direct measurement of single nanoparticles at high throughput. Combined with the previous section on binding and assembly, this dissertation lays the groundwork for future work on near-field optical forces which has great potential for improving our understanding of physics at the nanoscale.

BIOGRAPHICAL SKETCH

Dakota O'Dell was born in 1989 in Saratoga Springs, NY. He received his Bachelor of Science in Physics in 2011 from the University of Notre Dame, where he conducted research in nuclear, particle, and solid state physics. After graduation, Dakota joined the department of Applied and Engineering Physics at Cornell University to learn how to apply the methods of physics to solve practical problems. At Cornell, he joined the lab of Prof. David Erickson in Mechanical Engineering and worked closely with a diverse team of researchers in applied physics, mechanical engineering, information science, and nutrition. His graduate work covered a range of topics, but focused primarily on two main themes: optofluidic trapping and point-of-care medical diagnostic devices. He will complete his doctorate in Applied Physics in 2016. After graduation, he will be joining a biotechnology startup to try to commercialize some of his graduate research.

To my wife Kaylin, for her patience and unwaivering support

ACKNOWLEDGEMENTS

First, I would like to thank my advisor Prof. David Erickson. Although I came to Cornell with a strong background in research, I had no real experience in identifying a problem and designing a practical solution. My time in David's lab has been a pivotal experience for me, and I have learned so much– about science, about business, and most of all, about effective scientific communication. Thanks to David's mentorship, I know I now have the tools I need for a career in industry and I am very grateful for his guidance.

I would also like to acknowledge my graduate committee: Prof. Harold Craighead and Prof. Warren Zipfel of Cornell University. I appreciate all of their support and insight throughout the progress of my Ph.D.

I would also like to thank all of the members of the Integrated Micro- and Nanofluidic Systems Laboratory for helpful discussions and friendly advice over the years. I want to give special thanks to my collaborators on this dissertation work. I would like to thank Dr. Xavier Serey, who taught me how to trap my first particle and sat with me during the long nights in the cleanroom when I was learning electron beam lithography. I would also like to thank Dr. Pilgyu Kang, who was unfailingly selfless over the years and was always available to help, even when he wasn't asked. And especially, I would like to thank Perry Schein, who originally inspired the characterization techniques in the latter half of this dissertation. Perry and I have worked closely together for years to attack the same problem from different angles; without him, this work would not have been possible.

I also owe a great debt to my family. Without the encouragement of my mother, Veronica, and my father, Michael, I could never have made it to Cornell in the first place. They have been incredibly generous and supportive over the years.

Because of their many sacrifices and unconditional support, I have had a world of educational opportunities that they did not and for that I am eternally grateful.

And finally, I would like to thank my wife, Kaylin, for putting up with me for all these years. The life of a graduate student is neither easy nor comfortable and she has had to spend many nights alone while I was caught up in experiments. I appreciate all of her support while times were rough and I hope to return the favor in the years to come.

TABLE OF CONTENTS

LIST OF FIGURES

CHAPTER 1

INTRODUCTION: CENTRAL AIM AND SUMMARY OF RESEARCH

1.1 Central Aim

Nanoparticles are becoming increasingly important in a wide variety of areas, including drug delivery [1], catalysis [2], biosensing [3], and energy production [4]. Despite the growing need, however, there are significant gaps in our ability to understand and manipulate objects on the nanoscale [5–7]. One particularly promising method for enabling this manipulation is the use of near-field optics. Using techniques developed in nanophotonics, it is now possible to confine light into subwavelength dimensions and generate highly localized and highly tunable near-field optical forces. These forces can be very strong, up to tens of piconewtons, which is on the same order of magnitude as the thermal energy of the nanoparticles and the strength of a hydrogen bond [8, 9]. By applying these optical forces to nanoparticles and biomolecules in a controlled way, it is possible to probe their fundamental properties, manipulate reaction kinetics, and assemble new structures. I believe this methodology has great potential for improving our understanding of nanoscale interactions, particularly in areas such as biophysics and colloid science where existing theoretical models are still lacking in predictive power [10].

In this dissertation, I will demonstrate the first steps in designing a new toolbox of near-field optical techniques for controlling and characterizing single-particle dynamics. To do this, I will focus on efforts along two general themes: (1) the use of optical forces to directly control binding interactions and (2) the development of a high-throughput optical force spectroscopy platform for nanoparticle

characterization.

1.2 Brief Overview and Summary of Chapters

Each chapter of this dissertation covers a different application of near-field optical forces, with Chapters 2 and 3 focusing on controlling binding and Chapters 4 and 5 on high-throughput characterization. Chapter 2 details an experimental technique to use photonic forces to direct self-assembly of hybrid plasmonic-photonic resonators with greatly enhanced trapping potentials. Chapter 3 details the use of these hybrid resonators to manipulate antibody binding kinetics with highly localized optical forces. Chapter 4 investigates a statistical method for high-throughput characterization of nanoparticles using optical waveguides through a combination of analytic theory and Brownian dynamics simulations. Chapter 5 expands on this framework and details experimental data from applying this technique to various nanoparticle solutions of different sizes and materials. In Chapter 6, the major results of this dissertation are summarized, and suggestions are given for potential future directions of research.

Appendix A contains additional figures showing both the benchtop experimental setup used in Chapters 2 and 3 and the commercial setup used in Chapters 4 and 5.

1.3 Summary of Research Achievements

Aim 1: Fabrication of novel photonic-plasmonic resonator using directed self-assembly.

- A technique was demonstrated for assembling hybrid photonic-plasmonic nanotweezers by optically driving the adsorption of multi-walled carbon nanotubes onto a silicon waveguide.
- The hybrid resonators were then used for controllable trapping and releasing single polystyrene nanoparticles
- Finally, we demonstrate the ability to localize the deposition of metallic nanoparticles onto the resonators to form more complex nanostructures.

Aim 2: Localized control of protein adsorption onto surfaces using near-field optical forces

- A novel extension was developed for the popular Derjaguin-Landau-Verwey-Overbeek (DLVO) model to include the effects of optical forces.
- Optical resonators were used to opto-mechanically drive otherwise unfavorable adsorption reactions and the energy barrier of the reaction was measured.
- Opto-mechanical position control was confirmed by using optical resonators to attract antibodies into very close proximity to generate a FRET signal.

Aim 3: Development of a nanoparticle sizing technique using optical waveguides

- An analytic model was derived to obtain an estimate of the radius of a trapped nanoparticle from its dynamics within the trap
- The application of this theory was tested using Brownian dynamic simulations, demonstrating that nanoparticle sizing is in principle possible in only a few seconds of data per particle.

- A preliminary experiment was performed on a commercial waveguide setup to verify that the analysis method is viable in realistic experimental conditions.

Aim 4: Application of the nanoparticle characterization technique to a wider range of experimental samples

- R=260 nm and R=400 nm polystyrene particles were trapped and analyzed using the previous method to determine the size
- Additional theoretical work was applied to allow for orthogonal characterization of the polydispersity of the particle distribution as well as the interactions with the waveguide surface
- Preliminary experiments were also performed on unknown protein samples to show applicability for biological analysis.

CHAPTER 2

SELF-ASSEMBLED PHOTONIC-PLASMONIC NANOTWEEZERS FOR DIRECTED SELF-ASSEMBLY OF HYBRID NANOSTRUCTURES

2.1 Abstract

We demonstrate a technique for assembling photonic-plasmonic nanotweezers by optically driving the adsorption of multi-walled carbon nanotubes onto a silicon waveguide. The nanotweezers are then used to trap and release individual polystyrene beads. Additionally, we demonstrate the ability to localize the deposition of metallic nanoparticles to the intersection points between multiple carbon nanotubes with the goal of forming more complex hybrid nanostructures.

2.2 Introduction

The ability to confine and manipulate micron scale particles with light was first demonstrated by Ashkin et al. [11] in 1986 with the invention of optical tweezers. Optical gradient force based techniques have since enabled many pivotal advances throughout physics [12] and biology [13, 14]. Due to a well-known R^3 dependence of the optical power required [11], however, it is a significant technical challenge

Reprinted with permission from O'Dell, D., Serey, X., Erickson D., "Self-assembled photonic-plasmonic nanotweezers for directed self-assembly of hybrid nanostructures", Applied Physics Letters, 104 (4), 2014

to trap particles smaller than 100 nm with free-space optics. In the effort to trap smaller particles, several alternative nanotweezers paradigms have been recently developed. One method, pioneered by Kawata et al. [15] in 1992, relies on the electric field gradient created within the exponentially decaying evanescent field generated by total internal reflection. By spatially confining light in a photonic resonator, this optical gradient can be greatly amplified, allowing for stable trapping of particles on the order of 10 nm. Evanescent field optical trapping has been demonstrated with many types of photonic structures, including 1D photonic crystals [16], 2D photonic crystals [17], ring resonators [18], and slot waveguides [19].

In addition to near-field photonic traps, there has also been significant research into plasmonic optical trapping schemes. Plasmons, which arise from the quantization of plasma oscillations in metallic materials, allow sub-wavelength confinement of light and can also transcend the limitations of diffraction-limited optics. Plasmonic traps have been demonstrated by coupling light via prism into patterned arrays of metallic nanostructures, such as gold nano-pillars [20] and bowtie antennas. [21] While there are many advantages to using plasmonic excitation over a focused Gaussian beam, there are also some notable drawbacks to this approach. By dynamically adjusting the beam profile, free-space optical tweezers can offer both confinement and real-time 3D manipulation of particles– by contrast, a pre-patterned array of plasmonic traps offers sub-wavelength spatial confinement and inherent parallelization, but with a significant loss of dynamic control over the particles in each individual trap.

One way to address the comparative lack of control of near-field optical trapping is to combine the strengths of several techniques into a unified platform. We demonstrate a hybrid photonic-plasmonic trap, where near-field light from a

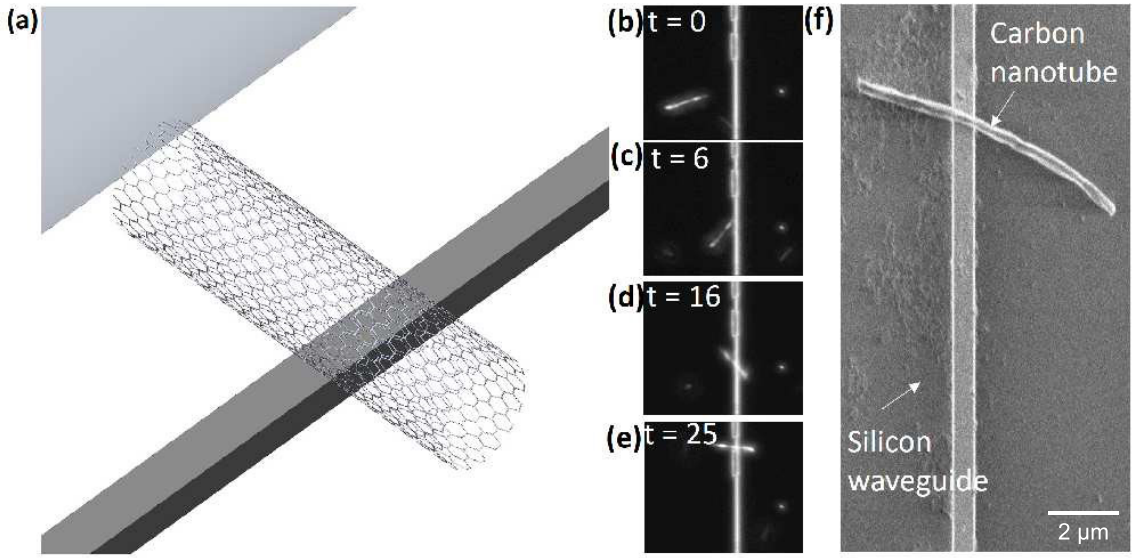

Figure 2.1: Assembly of multi-walled carbon nanotube enhanced optical nanotweezers. (a) A schematic of a plasmonically active carbon nanotube immobilized on a silicon waveguide. (b-e) The orientation and assembly of a carbon nanotube onto the waveguide by optical gradient forces. (f) An SEM micrograph of an assembled trap.

photonic waveguiding structure is coupled directly into a plasmonic resonance of carbon nanotube. The optical gradient force from the evanescent field is used to trap the plasmonic nanoparticle from solution, which then orients and self-assembles on the waveguide. A schematic of the hybrid trap and a demonstration of the assembly process is shown in Fig. 2.1. The coupling of the evanescent field to the plasmon resonance leads to a strong enhancement of both the electric field intensity and gradient near the nanoparticle surface, [22] and offers a convenient way to deliver light to a single nanoparticle on-chip with a high degree of precision. Moreover, the ability to vary the material properties, dimensions, and number of the nanoparticles used on the same chip offers a degree of customization which is not possible with pre-patterned arrays or nanofabricated structures.

2.3 Carbon nanotubes as plasmonic resonators

Because conventional plasmonic particles, such as gold and silver nanospheres, typically have plasmonic resonances in the optical frequency range, they are not well-suited for integration with silicon waveguides. Instead, we chose to use multi-wall carbon nanotubes (MWCNT) as the self-assembled resonators due to a host of unique optical and material properties. Depending on the configuration of carbon atoms, the band structure of CNTs can be either semiconducting or metallic. [23] In previous characterization studies, metallic CNTs have been found to display strong low-frequency plasmonic resonances with peaks near 1550 nm, [24] making them particularly suitable for this trap design. CNTs are also attractive for self-assembly due to their mechanical properties. CNTs are highly hydrophobic, [23] and hydrophobic dispersion forces will drive the nanotube to adsorb to the silicon waveguide. Because of this strong interaction, the assembled trap is robust to high flow speeds and flow switching, even in the absence of laser power.

Although multi-walled carbon nanotubes are rolled concentric shells of graphene, their optical properties are substantially different from both bulk graphite and graphene due to the unique low-dimensional geometry. For a heterogeneous solution of MWCNTs with many different numbers of shells, the frequency-dependent dielectric function is difficult to predict from first principles. To understand the expected optical properties of the CNT trap, we first consider the interaction between a single-wall carbon nanotube (SWCNT) and a silicon waveguide. Although SWCNTs can be either semiconducting or metallic, the field enhancement of the CNT trap relies on plasmon resonance effects which will only be present for the metallic type. Plasmons are a quantized oscillation of the free electron density in a material, and are thus highly dependent on the electron ge-

ometry and band structure. Unlike noble metals which exhibit visible-frequency peaks (corresponding to the resonance of a 3D electron gas), metallic SWCNTs are predicted to display unique plasmons in the near-IR due to collective oscillations of a 1D electron gas citeLin. These predicted resonance peaks are confirmed by experimental characterization of grown SWCNT films, which exhibit a strong extinction peak at energies below 1 eV [25]. Finite difference time domain (FDTD) simulations of a representative SWCNT on silicon were performed to predict the distribution of electric field strength for this resonance effect (Fig. 2.2(a)). For the simulated nanotube, the gradient of the electric field intensity is amplified within the evanescent field near the ends of the carbon nanotube, resulting in a greatly enhanced attractive optical force over the bare silicon waveguide near both these points. The frequency of the resonance peak is a function of the SWCNT geometry and can vary from around 0.6 eV to 1 eV [24].

The properties of MWCNTs are far more complicated, and the dielectric function will not, in general, have a single resonance peak in the near-IR. For a first-order approximation, we neglect the inter-shell interaction potentials and regard a MWCNT as a composite of concentric SWCNT shells which each display an independent plasmon resonance. [24] For a thick MWCNT with many layers, therefore, most of the shells will not be plasmonically resonant at any given wavelength. Those layers which are resonant, however, will dominate the optical response, and the majority of MWCNTs are expected to exhibit some plasmonic resonance at 1550 nm, even those that have vastly different geometries and numbers of shells.

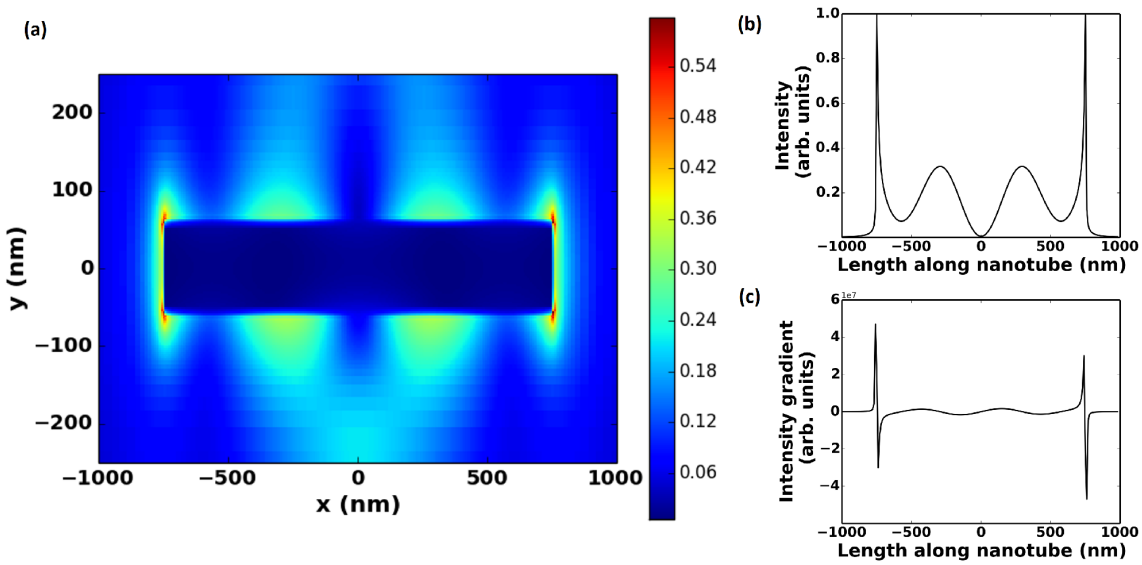

Figure 2.2: FDTD simulation of the CNT nanotweezers. (a) Electric field strength around a 1.5 micron nanotube atop a silicon waveguide at 1550 nm. (b) The predicted electric intensity along the major axis of the nanotube within the resonant evanescent field. (c) The intensity gradient along the major axis of the nanotube. The intensity gradient, proportional to the attractive optical force on a polarizable particle, is maximum just outside the two ends of the nanotube.

2.3.1 Assembling the resonator

To drive the self-assembly process, a tapered fiber is used to couple 1550 nm laser light into a silicon waveguide. A solution of 0.05% multi-walled CNTs in heavy water is prepared and ultra-sonicated for 20 minutes prior to each experiment to disperse the nanotubes. 0.5% Tween 20 (Sigma-Aldrich) surfactant is also added to prevent aggregation of the nanotubes during the experiment. The CNT solution is delivered to the waveguide through a Parafilm (Sigma-Aldrich) microfluidic channel mounted on top of the chip. The evanescent light from the waveguide polarizes the CNTs in solution and attracts them via an optical gradient force. The CNTs are rotated perpendicular to the waveguide due to the optical torque generated by

the electric field gradient [26], as seen in Fig. 2.1(b-e). When the nanotubes are brought close enough by the optical force, strong hydrophobic interactions cause irreversible adsorption to the waveguide surface. The silicon waveguide can then be used to evanescently couple light into the metallic nanotube and excite plasmonic resonances which greatly amplify the local electric field gradients near its surface. This amplification enhances the strength of the optical gradient force, allowing for stable trapping of particles as small as 10 nm. An SEM micrograph of a self-assembled CNT trap is shown in Fig. 2.1(f).

After assembling the CNT trap, we first confirmed the predicted plasmonic field enhancement of the MWCNTs by conducting optical trapping experiments with a non-uniform dispersity of carbon nanotubes under an infrared camera. After self-assembly onto the silicon waveguide, 1550 nm laser light was delivered into individual carbon nanotubes ranging in length from 3 to 10 microns with unknown shell structures. A strong resonance effect was observed for both short and long nanotubes, indicated by a high intensity infrared signal at the location of the nanotube and a strong attractive force on the other nanotubes in solution. When the same experiment was attempted replacing the metallic MWCNTs with 200 nm gold nanorods and 100 nm silver nanospheres (which do not have a near IR plasmonic resonance), the attractive force enhancement and high infrared intensity were not observed. Additional MWCNT experiments were also conducted on a hotplate without noticeable change in the attractive force, suggesting that the effect is indeed optical rather than purely thermal in origin.

2.3.2 Enhanced optical trapping

After investigating the plasmonic characteristics of the MWCNT trap, we demonstrated its effectiveness for near-field optical trapping. For these experiments, MWCNTs were immobilized one-by-one onto the waveguide surface to form a small cluster. A solution of tetramethylrhodamine isothiocyanate (TRITC)-tagged 520 nm polystyrene beads was flowed through the microchannel to be trapped. Fig. 2.3(a) shows the progression of a typical polystyrene bead trapping experiment over time at low power. After the beads are flowed into the channel, the 1550 nm laser is switched on. When a bead diffuses close enough to the resonant nanotube, the optical gradient force will attract it and hold it in a stable equilibrium position. Because the enhanced electric field extends along the surface of the micron-scale nanotubes, the CNT trap is able to stably hold many 520 nm beads at once. At low optical power input, the beads will be trapped near the nanotube ends on both sides of the waveguide, where the optical force is greatest (Fig. 2.3(a ii-iv)). If the laser is then switched off, the beads will diffuse back into solution (Fig. 2.3(a v)).

2.3.3 Directed self-assembly

In addition to amplifying the evanescent field for stable particle trapping, the CNT trap can also be used for directed self-assembly of nanoparticle complexes. In a bulk electrolyte solution, colloidal particle dynamics are governed by the interplay between attractive van der Waals dispersion forces and repulsive electrical double layer forces [27]. In the absence of optical power input, the electrostatic repulsion between CNTs and other colloidal particles is often strong enough to

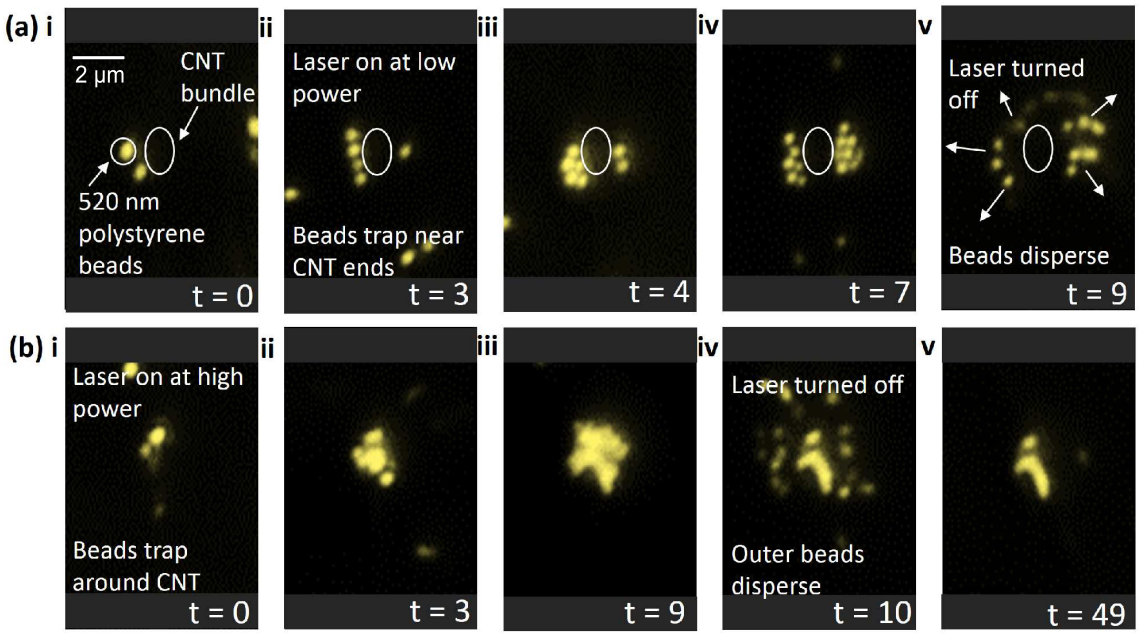

Figure 2.3: Optical trapping with the CNT nanotweezers. (a) Low power optical trapping. (i) Carbon nanotubes are immobilized onto the waveguide, and 520 nm polystyrene bead solution is flowed in. (ii-iv) When the laser is on at low power, the beads are attracted to the ends of the nanotubes and stably trapped on both sides of the waveguide. (v) When the laser is switched off, the beads are freed from the trap and diffuse back into solution. (b) High power optical trapping. (i-iii) At high power, the beads surround the whole CNT surface (iv-v) Even when the laser is switched off, the innermost beads stay irreversibly bound to the surface.

prevent adsorption. For the optical trapping experiments in the previous section, the equilibrium position is determined by the balance between the electrostatic repulsion and the attractive optical gradient force. When the laser power coupled in is sufficiently high, however, the amplified optical gradient force can overcome this double layer repulsion and bring the two particles into close enough proximity for hydrophobic forces to dominate and adsorption to occur. By using the silicon waveguide to couple light into a CNT, the trap can be used to coat the surface of the CNT with a wide variety of organic and inorganic particles. CNTs coated

with metallic beads have been investigated previously, both because of interesting optical resonance properties [28] and as a means to functionalize the CNTs for chemical [29] and biological sensing [30]. By delivering light with a silicon waveguide, these CNT/metal complexes can be created without prior chemical functionalization. As a demonstration of the potential for this type of assembly, we optically drive binding of both metallic and dielectric particles to the surface of the CNT enhanced traps.

To test the creation of CNT-dielectric nanoparticle structures, the polystyrene bead trapping experiments from the previous section were repeated at higher input optical powers. The progression of one such experiment is shown in Fig. 2.3(b). A bundle of several CNTs was self-assembled on trap, and the bead solution was flowed into the channel. The input laser power is then increased, and the beads are attracted to the trap. Unlike the low power experiments where the beads are held only at the two ends, the beads now accumulate around the entire surface of the nanotube (Fig. 2.3(b i-iii)). When the laser is switched off, the outermost layer of beads diffuses into the solution, but the layer which was closest to the CNTs does not (Fig. 2.3(b iv)). This surface coating of polystyrene beads is irreversibly bound to the carbon nanotubes, and remains indefinitely even in the absence of optical power (Fig. 2.3(b v)).

Because the resonant electric field is non-uniform across the CNTs, optical surface coating does not have to be an all-or-nothing process. For mid-range optical powers, it is also possible to bind particles only at the locations along the rod where the intensity gradient is highest. To show this, we demonstrate the selective assembly of CNT-metallic hybrid nanoparticle structures using 100 nm silver beads. After the assembly of the CNT trap, the microchannel is then used

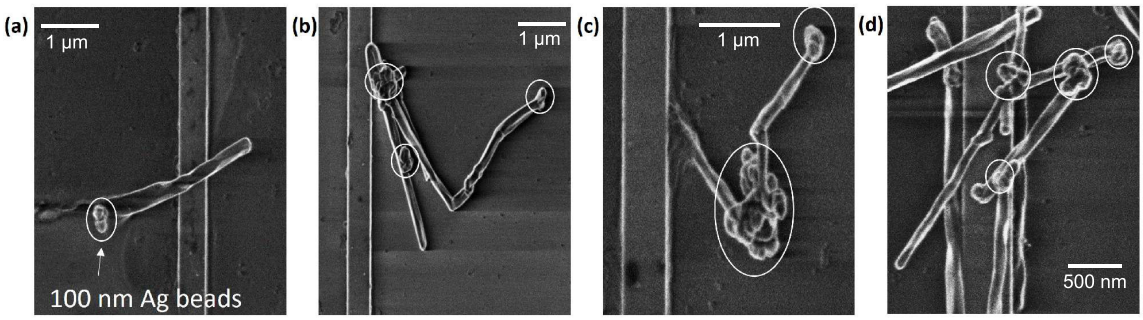

Figure 2.4: Binding of 100 nm silver beads to different carbon nanotube trap geometries. (a) For a single MWCNT, two silver beads bind near the end of the rod. (b-d) For more complicated multiple-CNT geometries, silver beads are found to bind both at the ends of the rods, and also at the intersection points between two or more rods.

to deliver a 0.01 mg/μL solution of 100 nm silver nanospheres. In the absence of optical power, no binding is observed between the silver and CNTs for over 30 minutes at this concentration. When the 1550 nm laser light is activated, the plasmonic resonance generates an attractive force and the nanospheres bind to the CNT, provided the power is high enough. The silver bead solution is left with the power on for at least 5 minutes to allow time for multiple binding events. For a single MWCNT, we would expect nanoparticles to bind most easily at the end of the nanotube. Fig. 2.4a shows an SEM micrograph of two silver beads which bound near the end of a single MWCNT during an experiment, supporting this hypothesis.

It is also illustrative to consider the assembly characteristics of a cluster of more than one nanotube. Because of the tendency of CNTs to aggregate when brought into close proximity, it is possible to use the evanescent field to assemble two or more CNTs into a complex geometry with different plasmonic characteristics. In such a system, two intersecting nanotubes might act as a nano-antenna, amplifying

the electric field in the nanoscale gap between them to be much stronger than at the end of a single rod. To investigate this possibility, CNT traps were assembled with two or three nanotubes each, and additional silver nanosphere experiments were conducted with these multi-tube traps. The results of three representative multi-CNT experiments are shown in Fig. 2.4b-d. In each case, we observe preferential binding of the Ag nanospheres at both the intersection points, confirming that the electric intensity gradient is enhanced at these locations. By leveraging this fact, the optical trapping and binding forces can be used to assemble more complicated nanoparticle structures (e.g., Fig. 2.4d). By carefully controlling the positions and orientations of the particles in solution, it would also be possible to direct the assembly of specific nanostructures with a predictable geometry.

Although there have been great advances in recent years in both plasmonic and photonic molecular nanotweezers, we believe there exists a need for a system which combines unique benefits of each approach. By using a combination of plasmonically active MWCNTs and silicon nanophotonic waveguides, we have demonstrated a plasmonic trap built on-chip with directed self-assembly. The CNT trap operates at 1550 nm in the standard telecommunications C-band; moreover, in contrast with photonic resonators such as 1D and 2D photonic crystals, the silicon waveguides used could be fabricated with standard CMOS-compatible photolithography. By exciting the plasmonic resonances of MWCNTs, these structures can be used both to attract and trap small molecules, and also to study and manipulate the interactions of carbon nanotubes with other materials at the nanoscale. We envision that the optically-driven surface adsorption employed could be used in the future to build complex nanoparticle structures and functionalize them for specific biological applications, as part of the evolving paradigm of assembling nanoscale systems from the bottom up.

CHAPTER 3

LOCALIZED OPTO-MECHANICAL CONTROL OF PROTEIN ADSORPTION ONTO CARBON NANOTUBES

3.1 Abstract

Chemical reactions can be described by an energy diagram along a reaction coordinate in which an activation barrier limits the rate at which reactants can be transformed into products. This reaction impedance can be overcome by reducing the magnitude of the barrier through the use of catalysis, increasing the thermal energy of the system, or through macroscopic mechanical processes. Here, we demonstrate direct molecular-scale control of a reaction through the precise application of opto-mechanical work. The method uses optical gradient forces generated in the evanescent field surrounding hybrid photonic-plasmonic structures to drive an otherwise unlikely adsorption reaction between proteins and carbon nanotubes. The adsorption of immunoglobulins on carbon nanotubes is used as a model reaction and investigated with an extended DLVO theory. The technique is also used to force a Forster resonance energy transfer between fluorophores on mismatched immunoglobulin proteins and is expected to lead to novel forms of chemical synthesis.

Reprinted with permission from O'Dell, D., Serey, X., Erickson D., "Localized Opto-Mechanical Control of Protein Adsorption onto Carbon Nanotubes", Scientific Reports 4, 2015

3.2 Introduction

The behavior of molecules in solution is governed by energy barriers, potential wells, and stochastic events. The progression of a chemical reaction is often described in terms of a reaction energy diagram that reflects changes in free energy along an abstractly defined reaction coordinate. In this framework, a reaction will occur if the reactants can acquire the necessary energy to overcome the activation energy barrier and proceed along the reaction coordinate towards the product state. This process can be accelerated by applying bulk kinetic energy in the form of heat, which raises the energy of the reactants relative to this barrier [31,32]. This can have a number of adverse effects, such as the acceleration of other undesired reactions decreasing the chemical efficiency and the denaturation of temperature-sensitive molecules, so alternative techniques are often necessary [33].

To counter the negative effects of heating, methods such as catalysis are used which reduce the activation energy by altering the intermediate states instead of adding energy to the reactants. In a catalytic process, a catalyst is introduced as an alternate reaction intermediate that changes the reaction pathway to one with a lower activation energy barrier [34]. While catalysis can greatly improve the rate of a reaction, it is ill-suited for studying the dynamics of a reaction because the reaction diagram itself is altered with a catalyst present [35]. Moreover, a particular catalyst will only accelerate certain reactions, and will be dependent on the molecules involved [35]. More recently, there has also been significant research into mechanical chemistry, in which mechanical forces are used to manipulate or induce chemical reactions [32, 36–38]. This is typically achieved with bulk mechanical processes such as grinding [38] and milling [32]. By grinding particles together with high force, mechanical stresses can cause deformations in the surface

structure which increase reactivity [37]. Reactions can also be similarly driven in bulk solution with vibrations, e.g. from ultrasonication [37]. On a more local level, individual nanoscale molecules such as DNA [39] and proteins [40] can be mechanically stretched and unfolded using forces generated by an AFM cantilever or by tethering them to larger nanoparticles, such as glass beads, which can then be pulled using optical or magnetic tweezers [39].

An alternative paradigm that uses mechanical work generated by near-field optical forces to overcome the activation barrier of a reaction without catalysis is demonstrated here. Light, and electro-magnetism in general, have been used previously to provide energy to certain reactions [41] or even to dope catalysts [42] without requiring a physical presence in the solution. Energy from absorbed photons has also been used to excite electrons to higher energy levels where they can react more readily or favor a specific conformation. Unlike thermal processes, however, these photochemical techniques require specific functional groups and electronic configurations, and do not generalize to other reactions. The opto-mechanical force demonstrated here is generated by polarizing dielectric particles, and does not require any specific chemical properties. Moreover, the force is strong enough to drive nanoscale particles without the need for an external tether which might change the conformation of the molecules of interest.

3.3 Results

In this work, light-mediated mechanical forces are used to locally modify the energy diagram of a protein adsorption reaction along the reaction coordinate without the use of a catalyst. The technique relies on optical gradient forces acting on

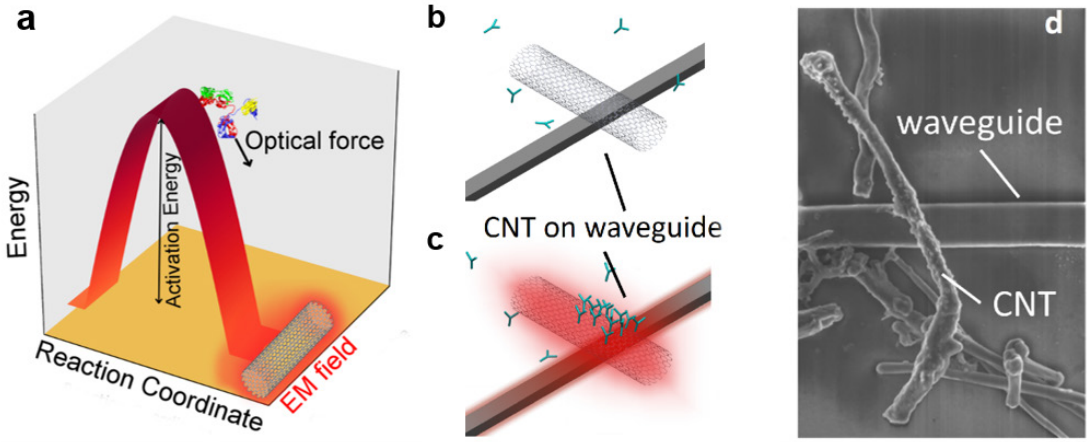

Figure 3.1: Schematic representation of the experiment. (a) Multi-walled carbon nanotube (MWCNT) on a waveguide. Few to no proteins (green Y) adsorb on the MWCNT in the absence of the electromagnetic potential. (b) With light shining, the metallic structure of the nanotube enhances the light intensity (red). Proteins now adsorb onto the nanotube. (c) Reaction diagram for the adsorption reaction. When the work done on the molecule by the optical force is large enough, the potential barrier corresponding to the DLVO repulsion is overcome. At very short distances between the nanotube and the protein, the reaction coordinate is no longer well approximated by the intermolecular distance, and optical forces become negligible compared to binding forces. (d) SEM image of a MWCNT on a silicon waveguide.

biomolecules in solution and on the adsorption of these molecules to hydrophobic surfaces. The exploitation of light to affect the motion of micrometer to nanometer scale particles was first pioneered by Ashkin when he invented optical tweezers in 1986 [11]. Since then, the optical gradient force has found numerous applications in optics, physics [12, 43] and biology [44]. Efforts to trap smaller molecules in solution have led to the recent development of molecular tweezers [45, 46] which allow proteins and other small elements to be trapped by nano-optics and nano-photonic structures. Non-mechanical aspects of the interaction of nano-optics with

molecules have also been investigated. For example, researchers have demonstrated the possibility to optically resolve molecular bonds with sub-nanometer resolution19. Other researchers have recently demonstrated the possibility to observe chemical reactions as they happen with nano-optical elements [47]. The present work builds on these efforts and is the first demonstration of the use of the electromagnetic gradient force, the mechanical force arising from the confinement of an electromagnetic field, to provide molecules with the necessary mechanical work to overcome the activation energy barrier standing between reactants and products in a reaction diagram.

In our first illustration of the use of these opto-mechanical forces to induce chemical reactions, we demonstrate the ability to control the adsorption of different forms of immunoglobulin proteins (Ig) onto carbon nanotubes (CNTs). Multiwall CNTs offer proteins a surface onto which they can adsorb (when forced into sufficient proximity) and also exhibit metallic properties which can expand and enhance electromagnetic fields [48,49]. When incident optical power couples onto the carbon nanotubes, an amplified evanescent field extends into the region surrounding the nanotube. This decaying field presents a strong electromagnetic intensity gradient which induces an optical gradient force on proteins in the vicinity of the CNT, as illustrated in Fig. 3.1. Except at very short distances, the reaction coordinate for the adsorption reaction is considered to be the separation between the two molecules, the same axis along which the optical gradient force acts. In the absence of these forces, the adsorption of the protein is prevented by double layer repulsion and by the presence of surfactant and blocking molecules at the surface of the CNTs. The adsorption experiments are performed at various incident optical powers, and the optical power at which the gradient force is just strong enough to pull the molecule through the activation energy barrier is recorded in each case.

3.3.1 Analytical theory

The reaction diagram was analytically modeled with an extended Derjaguin-Landau-Verwey-Overbeek (DLVO) theory for simplicity, despite some of its known shortcomings [10]. The DLVO potential energy, derived assuming a constant surface potential and extended to include hydrophobic interactions between a small sphere and a cylinder, is given by [50, 51]

$$U_{DLVO} = 64Rk_BTc_0\gamma_{0,p}\gamma_{0,CNT}\lambda_D^2 \mathrm{e}^{-\frac{z}{\lambda_D}} - \frac{AR_p}{6z} - C_h\mathrm{e}^{-\frac{z}{D_0}} \tag{3.1}$$

In this equation, U_{DLVO} is the potential energy of the colloidal interaction, R is the gas constant, k_B is the Boltzmann constant, T is the temperature, c_0 is the bulk ionic concentration, λ_D is the Debye length calculated as $\lambda^2 = RT\varepsilon/F^2c_0$ where ε is the buffer permittivity and F is the Faraday constant, z is the distance between the molecules, A is the Hamaker constant, R_p is the radius of the protein, C_h and D_0 are parameters in the hydrophobic extension of the theory, and $\gamma_{0,p}$ and $\gamma_{0,CNT}$ are the surface charge densities of protein and CNTs, respectively. The DLVO theory was further extended in Equation 3.2 to include the effects of the surfactant molecule and the mechanical action of light. Along the reaction coordinate, the energy diagram is now given by

$$U = U_{DLVO} - \frac{\alpha}{L_{ev}}|E_0|^2\mathrm{e}^{-\frac{z}{L_{ev}}} + \Delta TS_Tk_BT + NE_A\chi(z) \tag{3.2}$$

where U is the total potential energy of the reaction including optical forces, α is the polarizability of the protein, L_{ev} is the evanescent field length, E_0 is the electromagnetic field strength, S_T is the Soret coefficient of the protein, N is

the number of surfactant molecules that the protein needs to remove in order to dock on the nanotube, E_A is the activation energy required to remove the surfactant molecule, and χ is a Heaviside step function supported where the surfactant molecule resides. The second term of the equation is the electromagnetic potential well arising from the gradient force, and the third term corresponds to the thermophoretic effect [52]. The last term is introduced here and intended to model the presence of surfactant and blocking buffer molecules at the nanotube surface which are used in both dispersing the nanotubes in solution and preventing non-specific adsorption.

3.3.2 Controlled antibody adsorption

Experimentally, a silicon waveguide is used to transport the 1550 nm laser light to the nanotube immobilized on the waveguide surface, and the proteins are delivered through a microfluidic channel mounted on top of the chip, as drawn in Fig. A.1 in Appendix A. The light from the waveguide evanescently couples to the carbon nanotubes where it is amplified, forming a strong optical nanotweezer device which attracts nearby dielectric particles, as demonstrated in previous work [49]. In the present work, the optical gradient force arising from this light confinement is used to perform work along the reaction coordinate of an energy diagram to overcome the potential barrier which ordinarily prevents the reaction from occurring, as shown in Fig. 3.1(a). (For a schematic of the optical intensity near a CNT, see Fig A.2 in Appendix A.) Schematic views of the nanotube before and after the optical forces are used to drive the adsorption reaction are presented in Fig. 3.1(b),(c). The threshold power at which the adsorption starts is measured experimentally by observing the adsorption of the fluorescently tagged molecules

and is taken to represent the height of the energy barrier in the DLVO theory. Since changes in experimental conditions could have a substantial influence on the height of the potential barrier, the solution temperature and flow rate were held constant all across experiments at 294 K and 105 $\mu L/hr$, respectively. A control experiment was also performed where the solution was heated externally via hot-plate to rule out the possibility of a thermal mechanism for the adsorption. In this experiment, the temperature was varied from 294 K to 333 K without any observable adsorption onto the nanotube.

The opto-mechanical adsorption of fluorescently tagged IgM proteins onto CNTs is presented in Fig. 3.2. Prior to each experiment, multi-wall carbon nanotubes (outer radius 110-170 nm) were first immobilized on the silicon waveguides and exposed to blocking buffer (Starting Block TBS or SEA Block) for two hours. A dilution of 0.5 $\mu g/ml$ of Alexa 488 conjugated IgM proteins in a dilution of Phosphate Buffered Saline (PBS, dH2O, 0.5% Tween 20) was prepared prior to each experiment. Time-lapse fluorescent images of the nanotubes in the IgM solution were captured using a CCD camera with a one second exposure for one minute intervals every few minutes. In between these collection periods, the camera shutter was closed to prevent photobleaching from prolonged continuous exposure to the mercury lamp excitation. At the beginning of the experiment, no background fluorescence is visible, indicating that few to no IgM molecules are adsorbed on the nanotubes surface, as seen in Fig. 3.2(a). The input laser power is increased at approximately 10 minutes intervals and no adsorption is observed until it reaches the threshold power, as shown in Fig. 3.2(a-d). The readout power of the 1550 nm light is recorded by an optical power meter at the output of the chip and the total fluorescent intensity on the CNT is determined from the captured images using ImageJ. (For a schematic of the microchip within the imaging setup, see Fig. A.2

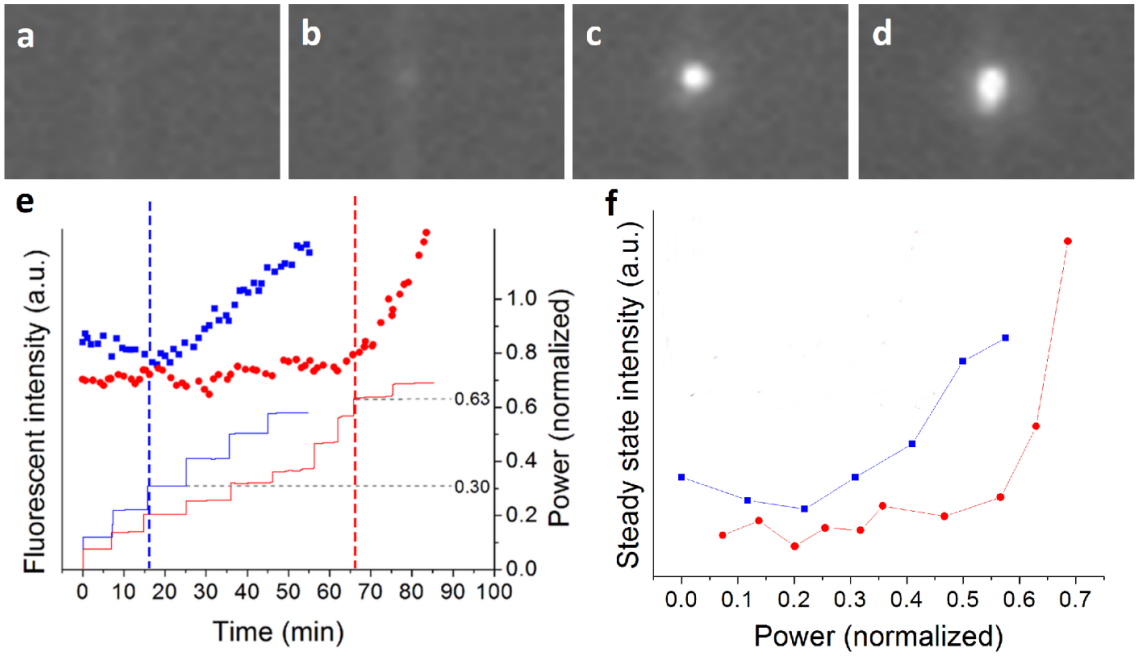

Figure 3.2: Aggregation of Alexa Fluor 488-conjugated IgM on a nanotube observed under fluorescence microscopy. (a-d) Fluorescent images before (a) and after (b-d) reaching the power threshold for adsorption. The bright spot is the aggregate. Each image is taken reaching steady state at the input power. (e) Plot of the measured fluorescent intensity in PBS 0.1X (blue dots) and in PBS 1X (red dots). Dashed lines at the bottom correspond represent the normalized power output. Vertical bars mark the time step when fluorescence begins to increase. (f) Plot of the steady state intensity as a function of coupled power for the same data sets as in (e).

in Appendix A.) The traces of the readout power and of the fluorescent signal are plotted in Fig. 3.2(e) as a function of time for two experiments in PBS 1X (red) and two in PBS 0.1X (blue). The colored dots represent the measured fluorescent intensity and the dashed lines are the power trace throughout the experiments. The steady state intensity, measured at the end of each power step, is also plotted in Fig. 3.2(f) as a function of the input power demonstrating that the adsorption only begins after the power reached a certain power threshold. The measured

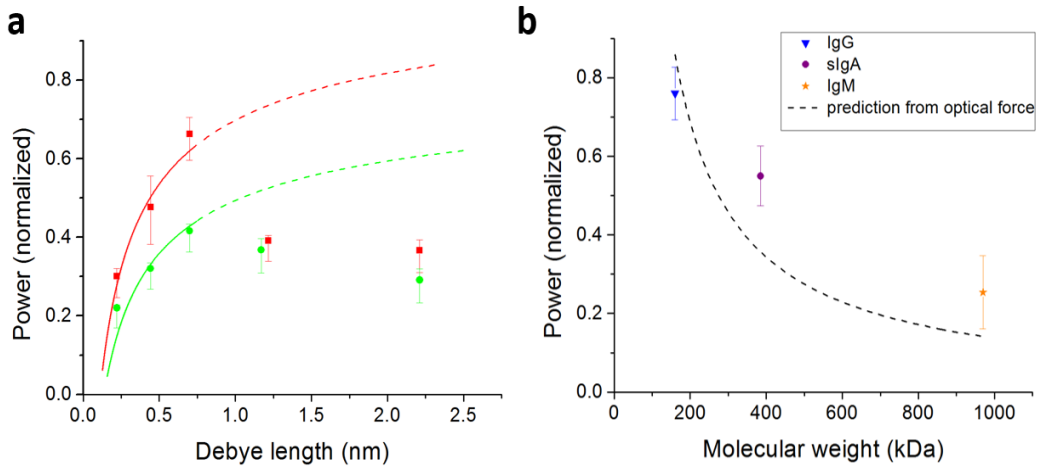

Figure 3.3: Power threshold at various salinities and protein masses for two polarizations of the incident light (green and red). (a) Measured power threshold for accumulation as a function of the Debye length of the buffer (colored dots) and estimate of the energy barrier height from the DLVO model (solid line) below 0.75 nm. Dashed lines: extension of the fit to the regions where the models assumptions fail. (b) Measured power threshold for accumulation as a function of the molecular weight of the immunoglobulin species used (colored dots). Dashed line: expected power threshold when the potential barrier is the same across species. Error bars: one standard deviation plus 5% lower bar to account for the discrete power steps.

threshold power depends on the coupling from the fiber to the waveguide and from the waveguide to the CNT which can vary from experiment to experiment. The measured powers are normalized by the power necessary to bring the temperature up from the bulk temperature to boiling, which always occurs at a given power density coupled in the carbon nanotube. Linearity of the heat and electromagnetic equations allow for such a normalization which therefore allows for direct comparison of experiments irrespective of the coupling conditions.

The effect of the Debye length on the activation energy of the adsorption reaction was measured by manipulating the concentration of the PBS buffer. The

power threshold at which the adsorption begins was recorded and is plotted in Fig. 3.3(a) as a function of the Debye length for experiments with two polarizations (green and red) along with the fitted activation energy as calculated from DLVO theory for different ionic strengths (solid curve). According to Equation 3.1, towards higher ionic strengths, or lower Debye lengths, the activation energy of the adsorption reaction should decrease due to dispersion forces. The applied electromagnetic potential necessary to overcome the activation energy and drive the reaction in Equation 3.2 should therefore decrease as well. Ignoring the effects of thermophoresis, the input optical power threshold is expected to map the activation energy from Equation 3.1. The activation energy is in qualitative agreement with the DLVO model used here at low Debye lengths (solid lines). Differences between the measured barrier height and the DLVO fit, particularly at higher Debye lengths (dashed lines), are attributed to the failure of the models assumptions and to changes in surface potential resulting from changes in pH [53]. The energy barrier was also measured for different immunoglobulin proteins as presented in Fig. 3.3(b) for two polarizations (green and red). Equation 3.2 indicates that the potential well depth is proportional to the polarizability, α, of the molecule which in turn scales with the mass, assuming a similar chemical composition. It is to be expected, therefore, that more optical power is necessary to overcome the same potential barrier for proteins with lower molecular weights. Fig. 3.3(b) presents the measured power threshold in PBS 10x for IgG, secretory IgA, and IgM with molecular weights 160 kDa, 385 kDa, and 970 kDa respectively. As expected, the necessary input power increases as the mass of the molecule decreases. The dashed curve presents the expected power threshold in the case where the potential barrier is the same across species.

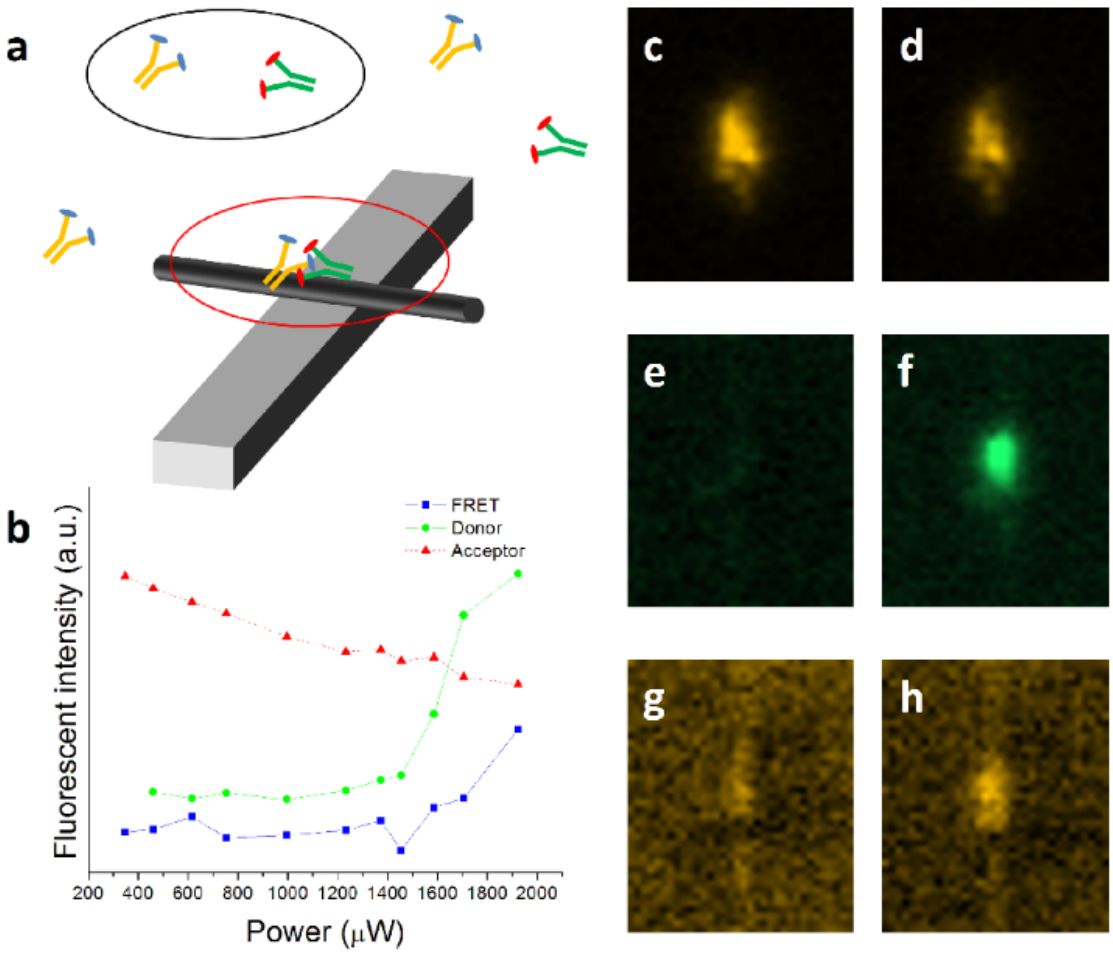

Figure 3.4: Forced proximity of mismatched IgM proteins. (a) Schematic. Black circle: useful collisions in solutions are rare. Red circle: in the potential well of the MWCNT, trapped molecules are confined to a smaller region making rare processes more common and more observable. (b) Trace of the intensity of the acceptor (red triangles), donor (green circles), and FRET (blue squares) fluorescent channels. The acceptor bleaches while donor and FRET remain unchanged until accumulation starts at which point they increase. (c-h) Pseudo-color contrast adjusted fluorescent images before (left column) and after (right column) accumulation. (c-d) FRET channel. (e-f) donor channel. (g-h) acceptor channel.

3.3.3 Optically driven FRET

The opto-mechanical chemistry technique was also used to drive a reaction between two mismatched immunoglobulin proteins. By forcing the molecules close together, a Forster Resonance Energy Transfer (FRET) signal was obtained between a donor (Alexa Fluor 488) and an acceptor (TRITC) conjugated to a goat anti-mouse IgM and a normal goat IgG, respectively. In the absence of optical forces, electrostatic repulsion would prevent the donor and acceptor from being close enough for a FRET reaction to occur. The observed FRET signal indicates that the opto-mechanical forces can bring the molecules into closer proximity than could otherwise be achieved. By creating a high local concentration of molecules in close proximity, the corresponding increase in collisions can force reactions or other exchanges between molecules which are otherwise unlikely to occur [54], as illustrated in Fig. 3.4(a). The acceptor molecule was first immobilized on the CNT, as seen in Fig. 3.4(c), and a blocking buffer (Starting Block TBS) was used overnight. Little to no background was found for the donor and FRET filters as seen in Fig. 3.4(e),(g) (some background is due to the blocking buffer and Tween 20). When the optical trap is activated, the donor-conjugated IgM starts aggregating (Fig. 3.4(f)) and a FRET signal arises from the forced proximity between the donor and the acceptor, which can be seen in Fig. 3.4(h). The intensity of the acceptor channel decreases steadily over the course of the FRET experiment due to photobleaching, as seen in Fig. 3.4(d).

3.4 Discussion

In this work, we have presented experimental evidence that near-field optical forces can be used to drive unlikely chemical reactions. Using fluorescently labeled antibodies, we find negligible protein adsorption to the carbon nanotube substrate without optical forces. When sufficient optical power is supplied from the laser, however, adsorption occurs rapidly and there is a sharp increase in the fluorescence signal. To account for this effect, we developed a novel extended form of the well-known DLVO theory of colloidal interactions which also accounts for optomechanical forces. As the model suggests, the repulsive potential due to the double layer charge will prevent the adsorption reaction from occurring under ordinary circumstances. When enough optical power is added, however, the attractive potential counterbalances the repulsive electric potential, and the proteins are pulled into very close range where hydrophobic forces dominate.

To confirm this effect, a series of experiments were performed to test the potential energy landscape under various conditions. By varying the salt concentration of the solution, we find that the power required to drive adsorption does vary as predicted by the extended DLVO model up to a Debye length of around 0.6 nm, but then decreases again for lower salts. The breakdown in the predicted trend is due at least in part to the limitations of the standard DLVO model in this regime. The DLVO theory treats the repulsive electrostatic forces and attractive Van der Waals forces as separable, an assumption which is not valid in biological salt concentrations [55]. Moreover, it neglects specific ion effects which can be particularly important in a salt mixture (like PBS) [10]. For this reason, the predictions of the theory are not expected to capture all of the system dynamics over the range of concentrations used; nevertheless, it is valuable to compare the driven

adsorption with a standard model of colloidal interactions to see where the predictions hold and where they do not. Despite the limited success of the model, the trend does match well with known qualitative properties of protein suspensions. As the salt concentration initially increases, the additional ions screen the charges on the proteins and reduce the attractive forces, a phenomenon known as salting in the proteins [56] Because the strength of the optical force is well-understood, opto-mechanically driven reactions can be used to probe the barrier height of a reaction even in cases where there is not a good analytic prediction. Because the polarizability of the molecule is linear with the mass, the required optical power is expected to increase as the mass of the antibody decreases if the adsorption is driven by the optical gradient force. Despite the breakdown in the salinity prediction, the mass trend agrees with this prediction well, suggesting that the dominant factor is the optical force. (For a discussion of additional thermal forces, see Appendix A.) An additional FRET experiment is performed which further supports that the antibodies are being forced over the repulsive barrier, as a FRET signal should only be visible if the donor and receptor are in very close proximity and does not occur in bulk solution without optical power.

From these results, we conclude that we have demonstrated for the first time the controlled driving of a reaction on a molecular scale using optically-mediated mechanical forces. Although the present work investigates protein adsorption to carbon nanostructures, this effect would generalize well to many other reactions, as the optical gradient force will act on any polarizable particle in solution and does not require a specific electronic structure. Along with other emerging methods [57, 58], this work is part of the changing paradigm challenging established means of interaction with molecules. It offers a new approach to study molecular reactions, develop methods in surface sciences and optofluidics [59–61], and study reaction

engineering, and may also provide opportunities in studying the structure-function relationship in large proteins or molecular clusters and in molecular mechanics.

3.5 Methods

The chip is composed of a silicon waveguide on a 3 μm SiO_2 on 500 μm Si wafer. The silicon photonic waveguides were fabricated using electron beam lithography techniques at the Cornell Nanoscale Facility. A microfluidic channel consisting of a glass coverslip, parafilm walls, and PDMS inlets/outlets was mounted on the chips prior to each experiment. To make the microfluidics, a rectangular channel was cut out from a single piece of parafilm using a CO_2 laser cutter. A glass coverslip with holes drilled at both ends was placed on top of the parafilm, and PDMS inlet and outlet blocks were attached at both ends using oxygen plasma bonding. The silicon chips were cleaned overnight in Nanostrip (Cyantek) between experiments to remove debris and parafilm residue. The 1550 nm light from a tunable laser (ANDO AQ4321) was amplified with an erbium doped fiber amplifier, delivered to the chip by a lensed fiber, and brought into physical contact with the chip through end-fire coupling to minimize power fluctuations. The chip was mounted on a microscope stage equipped for bright field and epi-fluorescence (CCD camera: Hamamatsu C4742-80-12AG). The CNT solutions were prepared by adding 5 mg of uncoated 0.01% MWCNT powder (outer radius 110-170 nm, Sigma-Aldrich product # 659258) and 0.5% Tween 20 to 10 mL heavy water and sonicating before each experiment for 20 minutes to inhibit aggregation. Fresh dilutions of PBS were also sonicated with 0.5% Tween 20 for 10 minutes prior to each experiment, and the pH of the buffer was kept between 6.8 and 7.3 to optimize Ig integrity. Alexa Fluor 488-conjugated IgM (Life Technologies), TRITC-conjugated IgG (Millipore), and

FITC-conjugated sIgA (Sigma-Aldrich), were diluted to 1 $\mu g/ml$ in PBS before each experiment. After adsorbing the CNT to the waveguide to form the trap, the protein solutions were flowed into the channel at a constant rate of 105 $\mu L/hr$ to replenish proteins and prevent the reaction rate from being limited by diffusion. The masses of the molecules were taken from the data sheets supplied by the vendors. After each experiment, the boiling power was measured using dark field microscopy and used to normalize each power curve. In the FRET experiment, a FRET cube was assembled to block the emission of the donor and the excitation of the acceptor.

CHAPTER 4

SIMULTANEOUS CHARACTERIZATION OF NANOPARTICLE SIZE AND PARTICLE-SURFACE INTERACTIONS WITH 3D NANOPHOTONIC FORCE MICROSCOPY

4.1 Abstract

The behavior of a nanoparticle in solution depends strongly on the particle's physical and chemical characteristics, most notably the particle size and surface properties. Accurately characterizing these properties is critical for quality control in a wide variety of industries. To understand a complex and polydisperse nanoparticle suspension, however, ensemble averaging is not sufficient and there is great need for direct measurements of size and surface properties at the individual nanoparticle level. In this work, we present an analysis technique for simultaneous characterization of particle-surface interactions and size using near-field light scattering and verify it using Brownian dynamics simulations. Using a nanophotonic waveguide, single particles can be stably held near the waveguide's surface by strongly localized optical forces. By tracking the dynamic 3D motion of the particle under the influence of these forces using an optical microscope, it is possible to extract the particle-surface interaction forces, as well as estimate the size and refractive index of the nanoparticle. Due to the strong light scattering signal, this method is viable for high-throughput characterization of particles as small as 100 nm in only a few

Adapted from an article O'Dell, D., Schein, P., Erickson D., "Simultaneous characterization of nanoparticle size and particle-surface interactions with 3D Nanophotonic Force Microscopy" which is under review at the time of writing.

seconds each.

4.2 Introduction

Nanoparticles have attracted significant interest in recent years due to a host of unique electronic, optical, and chemical properties [62–67]. These properties are governed largely by surface effects and are highly dependent on the particles size and surface area [68–71]. In many applications, the diameter of the particles used can have a dramatic effect on the particle's functionalityfor instance, whether the particles effectively screen out UV radiation [72], exhibit dangerous cytotoxicity in the body [68], or reliably pass through cell walls to enable targeted therapeutics [73]. It is critical therefore to determine the nanoparticle size distribution to ensure the safety and effectiveness of these engineered suspensions. This is especially difficult for heterogeneous suspensions where traditional sizing methods such as dynamic light scattering will average out a lot of the inherent polydispersity and can lead to misleading conclusions [74].

To address this, a number of new experimental techniques developed that focus on building up size distributions by measuring individual nanoparticles rather than a population averaged value [74]. These techniques, including single-particle tracking [75], have been used successfully to size a variety of metallic, dielectric, and biological nanoparticles [65, 76–79].

While single-particle size analysis is essential for understanding nanoparticle behavior, it does not tell the complete story. The interactions between nanoparticles and interfaces, for example, are highly dependent on the particles surface properties which can be difficult to predict from first principles [10, 69, 73]. There

are techniques which have been developed to directly measure the interactions of particles with surfaces, including a technique we have developed called Nanophotonic Force Microscopy (NFM) [80, 81]. This method offers very high resolution information on particle-surface interaction forces, but no information on the size of each particle.

For many applications, one would expect coupling between a particle's size and surface propertiesfor instance, when evaluating the long-term stability of a particle with an engineered surface coating [73]. In these situations, it would be highly desirable to have a technique capable of measuring both the size and surface properties of the same individual nanoparticle simultaneously. In this work, we develop a new single-particle tracking technique which is compatible with our previous nanophotonic force microscopy technique for force spectroscopy.

Single-particle tracking analysis relies on scattered light from particles which are freely diffusing in bulk solution. This allows for particle sizing, but not probing the forces on the particles in solution. Conversely, in NFM, the particles are held close to the surface by optical forces to allow for surface interaction measurements, and the particles are not freely diffusing. Using analytic theory and Brownian dynamics simulations, we will show that is still possible to extract the radius of a trapped nanoparticle by analyzing the particle's 3D motion on very short time scales with a high-speed camera. We will also demonstrate how the applied optical forces can be used to differentiate particles of the same size by their refractive index. Using simulations, we show that reasonable sizing accuracies (<10% error) can be achieved with a low-cost industrial camera and with as little as one second of video data per particle. This method is fully compatible with our previous NFM technique and both analyses can be run on the same video.

4.2.1 Single-particle Tracking Analysis

Prior to introducing our new methodology, we will review the method of diffusive sizing by single-particle tracking analysis (SPT). SPT is an optical analysis technique which works by tracking the Brownian motion of individual nanoparticles using light scattering [74]. Briefly, a laser is focused into a flow cell containing the nanoparticle suspension using a glass prism. The laser light scatters off the nanoparticles in the solution, and the scattered light from each particle is collected above the flow cell onto a CCD detector. The position of each particle in each frame can be determined with subpixel resolution using a particle localization algorithm. The motion of the particle can then be tracked frame-by-frame as the particle undergoes Brownian motion in order to find the mean-squared displacement [75]. For free (2D) diffusion, the mean-squared displacement is linearly proportional to the particle's hydrodynamic diffusion coefficient, D, by

$$MSD(r,t) = 2D\Delta t \tag{4.1}$$

where Δt is the elapsed time since the start of tracking. Using the Stokes-Einstein relation [82], this diffusion coefficient can be related to the particle's radius:

$$D = \frac{k_B T}{6\pi\eta R} \tag{4.2}$$

4.2.2 Nanophotonic Force Microscopy

The NFM technique works by pulling nanoparticles towards a waveguide surface using an attractive optical gradient force [80, 81]. The attractive optical gradient force is counterbalanced by surface forces (such as repulsive electrostatic forces, hydrophobic interactions, and steric hindrances) and the particle undergoes confined Brownian motion around a stable equilibrium height. Within the evanescent field of the waveguide, the optical intensity decays exponentially with height. As the particle fluctuates in height, it will scatter less light when farther from the surface and more light when nearer to the surface. Since the decay constant of the light intensity is known, the changes in intensity can be transformed into changes in height. If the light scattered by the particle is recorded over time, an equilibrium distribution of the heights can be found, and the potential well of the particle-surface interaction can be calculated using Boltzmann statistics. After the optical gradient component to the potential well is subtracted, a force-distance curve resulting from the surface force alone can be found. A schematic overview of this experimental procedure is shown in Fig. 4.1a-b. Readers interested in further details are referred to our previous publications [80, 81].

4.3 3D NFM Theory

Here, we describe a hybrid technique which combines NFM with a modified single-particle sizing method that accounts for the applied optical forces and surface effects. For this method, a nanoparticle is trapped within the evanescent field of the optical waveguide (Fig. 4.1a). The particle's position is then tracked in 3D space motion along the z-axis is determined by integrating the scattered intensity

(as in NFM) and motion in the x-y plane is determined by subpixel localization (as in SPT). The z motion can be used to find the force-distance curve, and the x-y motion can be used to find the particle size using a modified single-particle tracking analysis. This x-y motion is more complicated than the free diffusion case due to two major factors: (1) the influence of optical forces on the diffusive motion and (2) an anisotropic hindering of the diffusion coefficient near the surface. If these two effects can be accounted for, however, it is possible to use these complications to determine not only the particle size but also the refractive index. We will address the modifications necessary for both of these effects now.

4.3.1 Diffusion with optical forces

To combine the two measurement techniques, we must first consider the functional form of the optical forces resulting from the optical waveguide. A Rayleigh particle in the non-uniform evanescent field will experience four distinct forces: (a) an optical scattering force, proportional to the intensity of the light field and the particle's dielectric constant, (b) an optical absorption force due to momentum transfer by absorbing the incident light, (c) an attractive optical gradient force proportional to the gradient in intensity, and (d) a size- and height-dependent hydrodynamic drag force [83]. The magnitude of these forces is given by

$$F_{scat} = \frac{8\pi^3 I_0 \alpha^2 \varepsilon_m}{3c\lambda^4} \tag{4.3a}$$

$$F_{abs} = \frac{2\pi \varepsilon_m I_0}{c\lambda} Im(\alpha) \tag{4.3b}$$

$$F_{grad} = \frac{2\pi \nabla I_0 \alpha}{c} \tag{4.3c}$$

$$F_{drag} = 6\pi\eta R U_0 \tag{4.3d}$$

where I_0 is the optical intensity at the particle's position, and α is the optical polarizability, given by

$$\alpha = 4\pi \left(\frac{\varepsilon_p - \varepsilon_m}{\varepsilon_p + 2\varepsilon_m} \right) R^3 \tag{4.4}$$

where ε_p and ε_m are the permittivities of the particle and the medium, respectively [83].

A diagram of the relevant optical forces along all three dimensions, as well as the coordinate system used for the rest of the discussion, is shown in Fig. 4.1a. Although the optical force field is three-dimensional, it is useful to consider the projections along dimension separately for clarity.

Along the x-direction, the particle is propelled at terminal velocity by the balance of the optical scattering force and the Stokes drag force [84]. This motion is not used for sizing the particle, but it does rapidly push particles in a line through the field of view of the camera.

The optical gradient force along the z-direction can be used to balance the repulsive surface forces, exactly the same as in 1D NFM. The histogram of sampled heights can then be used to find the force-distance curve of the particle-surface interaction (Fig. 4.1b).

In additional to the downward optical gradient force used for the NFM measurement, however, there is also a component of the optical gradient force in-plane which points towards the center of the waveguide. Along the y-axis, this gradient force acts as a harmonic optical restoring force which is counterbalanced by Brownian fluctuations. The probability density function of the nanoparticle position over

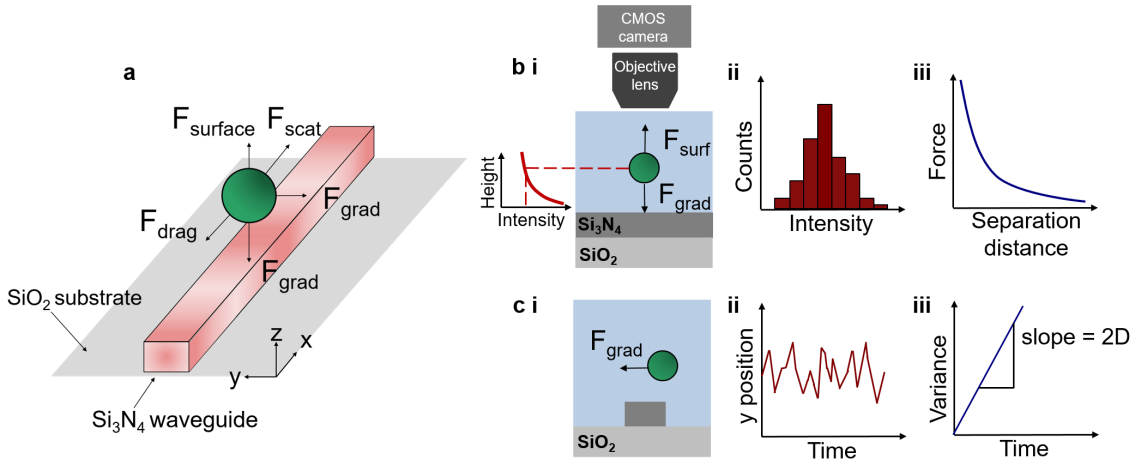

Figure 4.1: Overview of the 3D Nanophotonic Force Microscopy (3D NFM) technique. a) Free body diagram of the optical and non-optical forces which act on the nanoparticle captured in the evanescent field of a 1D nanophotonic waveguide. As the particle moves within the exponentially-decaying field, it scatters light which is detected by an industrial CMOS camera above. The inset coordinate system will be used for the rest of this work. b) In the z direction (perpendicular to the waveguide surface), the particle fluctuates in a potential well created by attractive optical and repulsive surface forces. The magnitude of the surface forces can be found by tracking the height-dependent scattering intensity over time, finding the combined potential well, and subtracting the optical contribution. c) Along the y direction, the particle fluctuates stochastically in a harmonic potential due to confined Brownian motion. The x-y position of the particle is found by localizing the centroid of the light scattering pattern, and the y position is tracked over time. The motion over short time intervals is used to extract a diffusion coefficient and eventually the particle size.

time is governed by the Smoluchowski equation for a harmonic biasing force [85]:

$$\frac{\partial}{\partial t}P(y,t|y_0,t_0) = D\left(\frac{\partial^2}{\partial y^2} + \frac{k_{trap}}{k_B T}\frac{\partial}{\partial y}y\right)P(y,t|y_0,t_0) \tag{4.5}$$

where D is the diffusion coefficient and k_{trap} is the spring constant of the effective harmonic potential.

Following the results of Lindner et al. for tethered Brownian motion [85], the solution to this partial differential equation is a Gaussian function with a variance that grows over time and depends on both k_{trap} and D:

$$\sigma^2(\Delta t) = \frac{k_B T}{k_{trap}}\left[1 - exp\left(-\frac{2(k_{trap}D)\Delta t}{k_B T}\right)\right] \tag{4.6}$$

Both k_{trap} and D will vary with the size of the particle. k_{trap} also depends on additional parameters, such as the optical intensity and the refractive index of the nanoparticle material. Since these parameters are not always known a priori, it is desirable for sizing to decouple these effects and find only the diffusion coefficient. This can be accomplished by observing the particle motion for very short time lags where the particle has not yet been significantly influenced by the restoring force. Taking a first-order Taylor approximation of Eq. 4.6, we find that

$$\sigma^2(\Delta t) \approx \frac{k_B T}{k_{trap}}\left[\frac{2k_{trap}D\Delta t}{k_B T}\right] \approx 2D\Delta t \tag{4.7}$$

for short time lags. In this limit, the variance of the displacement is linearly proportional to the lag between measurements. With a sufficiently fast frame rate, therefore, it is possible to determine an effective diffusion coefficient by fitting a line through the first three frame lags and finding the slope (Fig. 4.1c).

4.3.2 Brownian dynamics simulations

In conventional single-particle tracking analysis, the particle undergoes free Brownian motion in two dimensions [82]. Under these conditions, the accuracy of the reconstruction does not depend on the position sampling rate and an accurate diffusion coefficient can be found by tracking a single particle for relatively long times at a relatively low frame rate (e.g. recording for 60 s with a 30 FPS CCD detector) [76]. As seen in Eq. 4.6, however, there is an explicit time dependence when the particle is held within the evanescent field. If the sampling rate is too low, the observed dynamics will be a combination of motion due to diffusion and motion due to the optical restoring force which would be difficult to decouple. As a result, our modified 3D NFM technique must operate at significantly higher frame rates than the traditional configuration allows.

To evaluate the viability of SPT for nanoparticle sizing with optical forces, we performed a series of 1D Brownian dynamics simulations at a sampling rate of 5000 FPS. This frame rate is achievable with many industrial CMOS cameras which is critical for a low-cost, high-throughput analysis method [86].

A representative Brownian dynamics simulation of an R=150 nm particle is shown in Fig. 4.2. Fig. 4.2a shows a one second generated Brownian trajectory of motion within the harmonic potential along the y axis, sampled at 5000 FPS. Starting from each frame, the displacement of the particle after n=1,2,3 frames are calculated. These displacements will be normally distributed, and the variance of that distribution can be plotted as a function of time lag, as suggested by Eq. 4.6. As seen in Fig. 4.2b and c, the chosen sampling rate of 5000 FPS is fast enough that the variance grows linearly in time, corresponding to the diffusive regime. A line is then fit to the first three points of the variance curve, the slope of which is

twice the effective diffusion coefficient.

For this representative particle, we extract a diffusion coefficient of 0.69 $\mu m^2/s$ from a ground truth value of 0.73 $\mu m^2/s$ for a 5.5 % deviation. This error could be reduced by increasing the frame rate further or taking data for a longer interval, but 5000 FPS for one second gives a conservative estimate of what is possible in a realistic experiment. Note that if the frame lag is too long (e.g., even 5-10 ms), a linear fit to the remaining data in Fig. 4.2b will greatly underestimate the diffusion coefficient and the analysis technique will not be reliable.

4.3.3 Diffusion near the surface

Due to the close proximity of the nanoparticle to the waveguide surface, the inverse relationship between R and D predicted by the Stokes-Einstein relation does not hold [87–89]. Instead, it is well-known that the diffusion coefficient very near to a wall is hindered by hydrodynamic effects, and the effective diffusion coefficient of the particle is both anisotropic and height-dependent. Along the y direction, this hindered diffusion coefficient is given by Faxen's law:

$$\beta_y(z) = 1 - \frac{9}{16}\left(1+\frac{z}{R}\right)^{-1} + \frac{1}{8}\left(1+\frac{z}{R}\right)^{-3} - \frac{45}{256}\left(1+\frac{z}{R}\right)^{-4} - \frac{1}{16}\left(1+\frac{z}{R}\right)^{-5} \quad (4.8)$$

$$D_y(z) = \beta_y(z) D_{bulk} \quad (4.9)$$

where z is the height of the bottom of the particle above the surface, R is the radius of the particle, and D_{bulk} is the ordinary Stokes-Einstein diffusion coefficient far from the wall [87]. This function is plotted as a function of height for three particle sizes in Fig. 4.3a.

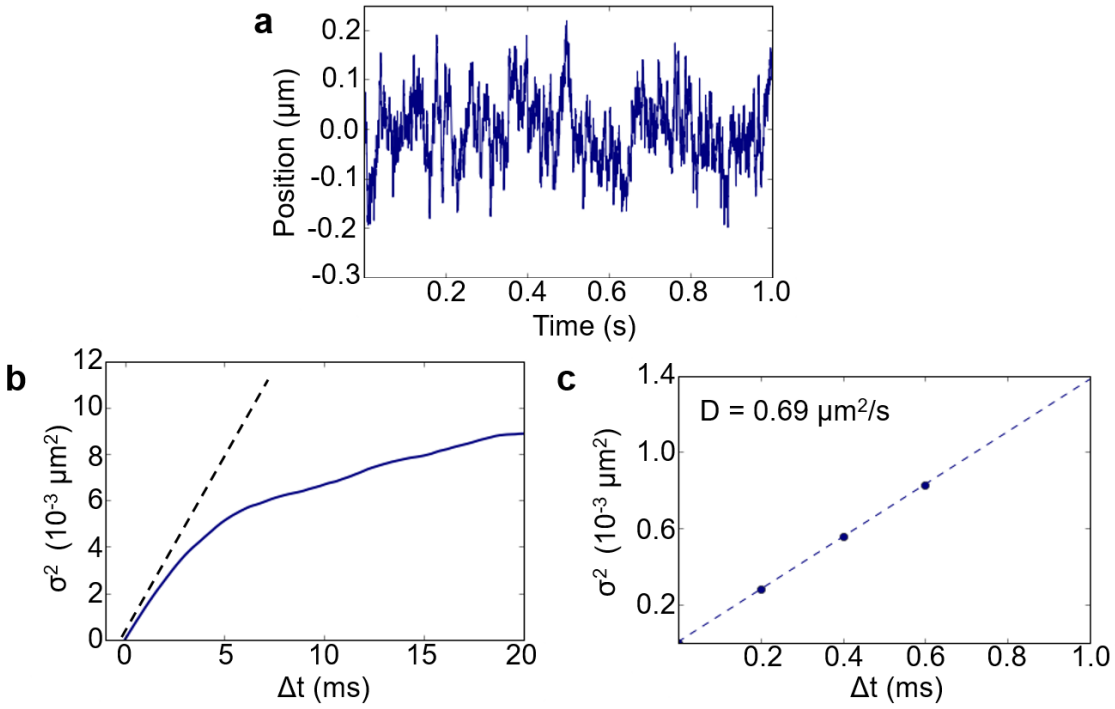

Figure 4.2: Brownian dynamics simulation to demonstrate the hydrodynamic diffusion analysis technique. a) The 1D Brownian trajectory of a nanoparticle with radius 150 nm in the harmonic potential 20 nm above the optical waveguide. To approximate a reasonable experimental implementation, the particle is sampled at 5000 FPS for one second. b) The variance of the particle motion as a function of time lags between frames. In the short time lag limit, the motion can be approximated as purely diffusive and the variance will be linear in time. c) A linear fit to the first three time lags (i.e., the displacement after 1 frame, 2 frames, and 3 frames) to determine an effective diffusion coefficient.

This relationship has been verified experimentally using a variety of measurement techniques [87–89]. In general, the hindered diffusion coefficient is a nonlinear function of the height of the particle above the waveguide surface as well as the particle's radius. For a particle of an unknown radius at an unknown height, therefore, it is not possible to uniquely determine the size directly from the diffusion coefficient. If the distance from the bottom of the particle to the waveguide is

known, however, this expression can replace Stokes-Einstein to relate the effective diffusion coefficient directly to the particle's radius, achieving the same simplicity as the free diffusion analysis used in SPT.

Fig. 4.3b shows the diffusion coefficient as a function of size as predicted by Faxen's law. For a given height (defined as the distance between the bottom of the particle and the waveguide surface), the measured diffusion coefficient is sufficient to extract the particle radius. If the height is completely unknown, however, there is not a one-to-one relationship; a 50 nm particle at the surface, for example, will diffuse similarly to a 150 nm that is 100 nm away. In Fig. 4.3c, Brownian dynamics simulations were performed to confirm that nanoparticles with radii from 50 to 300 nm are distinguishable from their measured diffusion coefficients. For each size, 100 particles were simulated for one second each using the predicted diffusion coefficient at a fixed height of 20 nm, and the diffusion coefficients were extracted using the method outlined in Fig. 4.2. As seen from the simulation results, the stochastic nature of the Brownian dynamics simulations adds some uncertainty to the measured diffusion coefficient; nevertheless, one second of data at 5000 FPS is sufficient to recover the input diffusion coefficients and separate the particles by radius.

4.3.4 Manipulating the particle height

In the previous analysis, it was shown that the particle size can be determined from the measured diffusion coefficient as long as the height above the surface is known. While variations in height are relatively easy to determine, absolute height is more difficult. Although the amount of light scattered by the particle varies exponentially with height, the absolute height above the surface cannot be

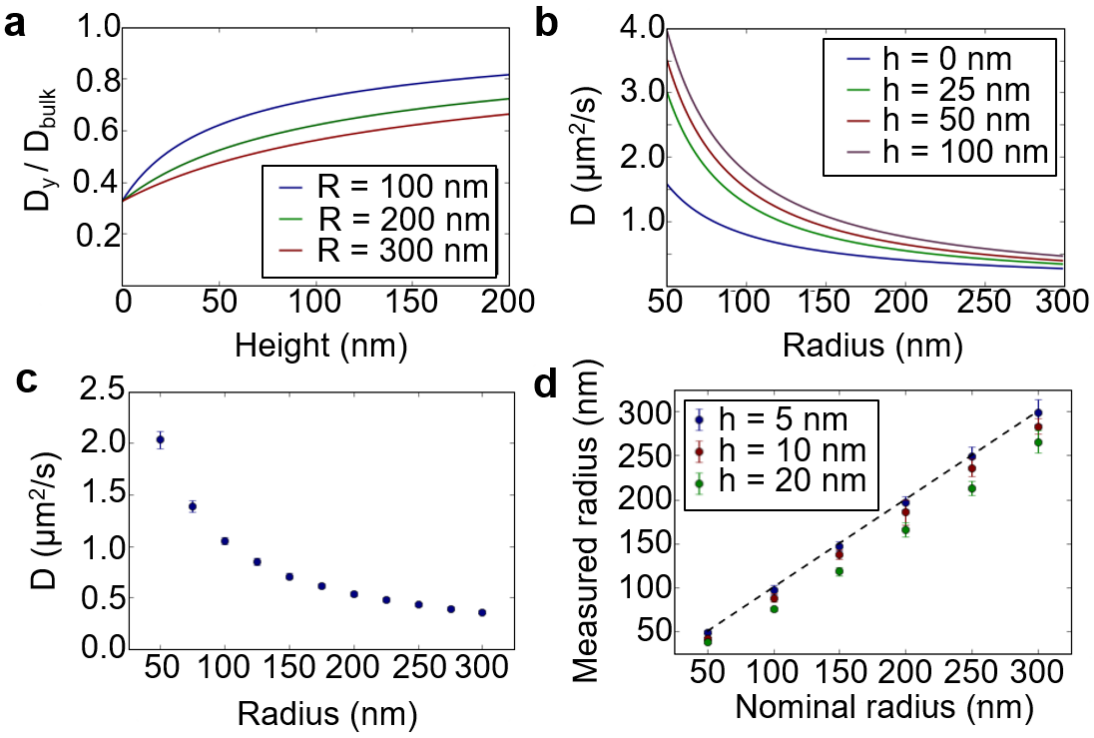

Figure 4.3: Particle size estimation incorporating hindered diffusion theory. a) The hindered diffusion coefficient for nanoparticles of a given size above the surface, according to Faxen's law. The degree of hindering depends on both the size of the particle and height above the surface. b) If the height above the surface is known, the particle radius can be uniquely determined from the measured diffusion coefficient. c) Measured diffusion coefficients for N=100 simulated particles at each size using the short time lag diffusion method outlined in Fig. 4.2. The equilibrium height is 20 nm above the waveguide surface. d) The error in measured radius for particles which are considered to be on the surface but are actually at a height h above the surface. As the height above the surface increases to 20 nm, the radius is systematically underestimated, but by less than 50 nm. N=10 particles per size. Error bars represent one standard deviation. h=0 is defined as direct contact between the waveguide surface and the bottom of the nanoparticle.

calculated without knowing the optical intensity at the waveguide surface. In total internal reflection microscopy, this is often accomplished by increasing the salt concentration irreversibly sticking the particles to the surface at the end of an experiment [88]. This is not compatible with high throughput analysis, as it would contaminate the surface of the chip and prevent further particles from being analyzed.

For our waveguide-based light scattering technique, however, the equilibrium height above the surface is not fixed, but depends on the balance of optical and surface forces. The magnitude of the optical force can be tuned by varying the input optical power in the waveguide. By increasing the input power enough, a nanoparticle in the evanescent field of the waveguide can be driven into contact or near-contact with the waveguide surface. In this regime where $h/R \rightarrow 0$, the hindered diffusion coefficient parallel to the waveguide converges towards a common value of 0.324 for all values of R. Incorporating Eq. 4.9, this yields a simple inverse relationship between the measured diffusion coefficient from the linear fit and the particle's radius

$$R \approx 0.324 \left(\frac{k_B T}{6\pi\eta D_{measured}} \right) \tag{4.10}$$

For an appropriately tuned optical power, it is possible to estimate the size of each particle as well as measure the particle-surface interaction potential very near to the wall. The systematic error in the calculated radius will depend on how close the nanoparticle can be brought to the wall without sticking irreversibly. Fig. 4.3d shows a size analysis of simulated particles of different nominal sizes. For each size, the approximation that the particle is very near to the surface is used, and the actual height above the surface is increased to test the error in the final value

as a result of that assumption. As the height above the surface increases, the size of the particle is systematically underestimated, but remains within 50 nm of the nominal radius for a gap height of 20 nm. The effect of this systematic bias is most significant for the smallest particles, but can be diminished by increasing the optical power to shift the equilibrium height closer to the surface.

4.3.5 Refining the size estimate

For applications where only coarse binning by size is needed, the approximation in Eq. 4.10 may be sufficient. For higher precision, however, additional techniques may be employed. From the exponential decay of the evanescent field, we know that the ratio of the scattered intensity at any two points can be used to find the distance between them:

$$\Delta z = -d * ln\left(\frac{I(z_2)}{I(z_1)}\right) \tag{4.11}$$

The small but measurable changes in height about an equilibrium position z_{eq} form the basis of the NFM force spectroscopy technique [81]. If the optical power into the waveguide is cycled periodically, however, the particle will jump between multiple equilibrium positions, $z_{eq,1}$, $z_{eq,2}$, $\ldots z_{eq,n}$. Due to hindered diffusion, the effective diffusion coefficient for the particle at each height will depend nonlinearly on the height and particle size. By sequentially recording the motion of a single particle about N equilibrium positions, therefore, it is possible to derive a nonlinear system of equations

$$
\begin{aligned}
D_i &= \beta_{y,i} D_{bulk} \\
&= \left[1 - \tfrac{9}{16}\left(1+\tfrac{z_i}{R}\right)^{-1} + \tfrac{1}{8}\left(1+\tfrac{z_i}{R}\right)^{-3} - \tfrac{45}{256}\left(1+\tfrac{z_i}{R}\right)^{-4} - \tfrac{1}{16}\left(1+\tfrac{z_i}{R}\right)^{-5}\right] \tfrac{6\pi\eta R}{k_B T}
\end{aligned}
\tag{4.12}
$$

$$
z_j = z_i + \Delta z_{ij} \tag{4.13}
$$

The difference between the equilibrium heights Δz_{ij} can be found from the ratio of the power normalized intensities by

$$
\Delta z_{ij} = -d * ln\left(\frac{I(z_i)/\langle P_i \rangle}{I(z_j)/\langle P_j \rangle}\right) \tag{4.14}
$$

where P_i is the optical input power for the i^{th} equilibrium height. Although this system of equations does not have a generalized analytic solution, the radius and heights can still be found numerically with a nonlinear optimization scheme to improve the accuracy of the initial guess for R based on the coarser model. Ideally, many heights would be used to maximize the fitting accuracy, but the accuracy of both the diffusion and force information at each height will decrease if the observation time is too low. Using the waveguide architecture from our previous work, we found that particles were observable for an average of 3-5 seconds each and require 3000 frames for accurate statistics [80]. Coupled with the sampling rate of 5000 FPS, this would allow for at least 5 powers to be sampled with the minimum 3000 frames at each height. Fig. 4.4a and 4.4b show the results of a simulation where a single 150 nm and 300 nm particle are sampled at 5 different heights for one second each, respectively. For the 300 nm particle, the closest gap distance between the particle and the surface was set to 25 nm. A minimum gap height of 29 nm and a measured radius of 317 nm were obtained from a nonlinear least squares fit to the five effective diffusion coefficients for a 5% error in the estimated

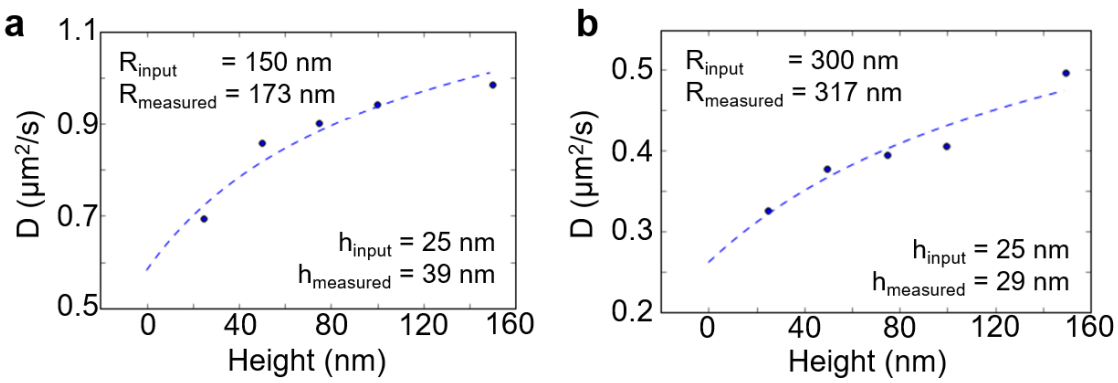

Figure 4.4: Refining the particle size estimate. Representative simulation of (a) an R=150 nm particle and (b) an R=300 nm particle measured at 5 different heights for one second each. Using the measured diffusion coefficients and the relative displacements between the heights, the radius and the absolute height are estimated through a nonlinear least squares fit. The relative error in the size estimate decreases for larger particles, as the hindered diffusion coefficient is less sensitive to small fluctuations in height.

size. If the camera frame rate were higher, more powers could be sampled that meet the 3000 frame threshold and the accuracy of this size estimation could be further improved. NFM analysis of the multiple powers data would also yield a separate potential well centered around each height. The resulting potential wells could then be stitched together to give a fuller picture of the surface forces up to 150 nm above the waveguide surface.

4.3.6 Optical and material characterization

Using the diffusive analysis technique from the previous section, it is possible to determine the hydrodynamic size of individual nanoparticles because the dynamics of the particle at sufficiently short time lags do not depend on the magnitude of

the optical forces. For unknown samples, the optical properties of the particles, e.g. the refractive index, do not need to be known a priori in order to determine the size. Nevertheless, the optical properties of the particles are often critically important and can, for instance, help to differentiate subpopulations which are similar in size but composed of different materials. Taking Eq. 4.6 and looking only in the long time limit, we find that the variance depends only on the trap stiffness

$$\sigma^2(\Delta t \to \infty) = \frac{k_B T}{k_{trap}} \tag{4.15}$$

matching the predictions of the equipartition theorem. This trap stiffness can then be compared with the analytic expression for the optical gradient force along the y-axis:

$$F_{grad,y} = \left(\frac{2\pi}{c}\nabla I\right)\alpha = k_{trap} y \tag{4.16}$$

where is the optical polarizability of the particle, as defined in Eq. 4.4. The polarizability of a single nanoparticle can then be found either by calculating the pre-factor in Eq. 4.16, or by normalization between multiple particles [90]

$$\frac{k_{trap,j}}{k_{trap,i}} = \frac{\sigma^2_{y,i}}{\sigma^2_{y,j}} = \frac{\alpha_j}{\alpha_i} \tag{4.17}$$

Since R can be found through the non-optical diffusive characterization from the previous section, this allows direct comparison of the refractive indices of the particles. This is especially useful for distinguishing metallic and dielectric

nanoparticles of similar sizes, as the difference in optical polarizability can be several orders of magnitude [91].

Fig. 4.5 shows a representative simulation which demonstrates the decoupling of size and optical properties for particles with two different polarizabilities. For this demonstration, two particles are simulated at the same height, one with a polarizability α and one with a polarizability 4α. Fig. 4.5a shows the histogram of particle positions in the long-time limit after the particle has reached equilibrium due to the optical gradient forces. In this regime, the measured variance in the particle position is inversely proportional to the polarizability and independent of the diffusion coefficient, as predicted by Eq. 4.17. In Fig. 4.5b, the same two simulated particles are analyzed for only the short time lags, as in Fig. 4.2. In this limit, the extracted diffusion coefficients are comparable despite the stark difference in polarizability. By analyzing the same raw particle trajectory in the two regimes, it is possible to independently measure both k_{trap} and D. For a heterogeneous sample, this can be used to distinguish subpopulations of particles that are similar in size but not in refractive index. This could be useful in screening out unwanted contaminants in the solution, such as dust particles or oil droplets, which could otherwise affect the size distribution accuracy.

4.4 Experimental verification

To demonstrate that the proposed sizing method is indeed viable for high-throughput industrial use, we performed an experiment using a low-cost industrial CMOS camera (aCA2000-165um, Basler AG) and a commercially-available optofluidic waveguide chip (Optofluidics, Inc.). For this experiment, we optically

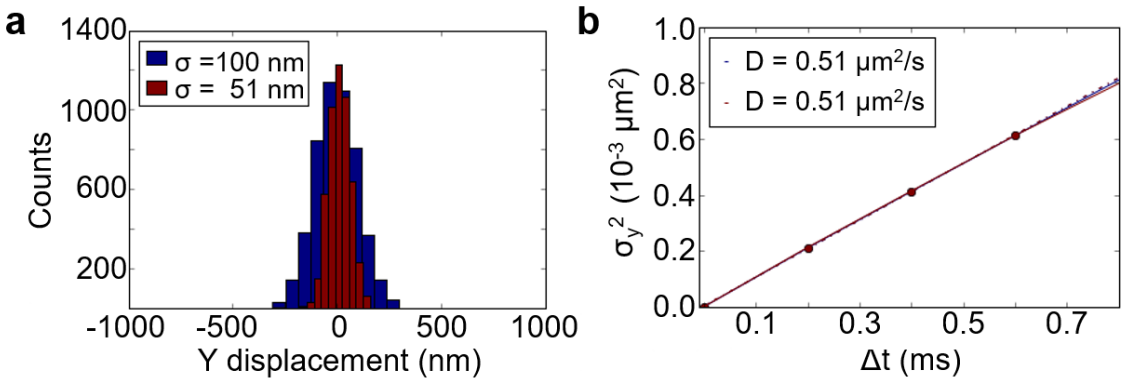

Figure 4.5: Separation of particles with different optical polarizabilities. a) Determination of the trap stiffness through long-time equilibrium data of two simulated particles sampled at 5000 FPS for one second. The optical trap stiffness (proportional to the variance) is 4 times larger for the red particle than the blue one. b) Hydrodynamic sizing analysis for the same two particles using short time lag diffusion. Although the difference in polarizability is clear from the long-time data, the short-time diffusion is independent of the magnitude of the optical force and the measured diffusion (and radius) is similar for both particles.

trapped an R=150 nm NIST traceable polystyrene bead over the surface of an optical waveguide and recorded the scattered light intensity using a 20x objective on an optical microscope at 3000 frames per second. The radius of 150 nm was selected to match as closely as possible the simulations in Fig. 4.2. The position of the trapped particle was then tracked in two dimensions using the MOSAIC ParticleTracker plugin for ImageJ [92].

Fig. 4.6a shows a still image of the light scattered by the particle during the experiment.The red circle shows the position of the particle as determined by the spot tracking algorithm. Fig. 4.6b shows the trajectory of the particle over 3 seconds (or, equivalently, 9000 frames). The motion of the particle along the two tracked dimensions agrees well with the predictions of both the analytic theory and the

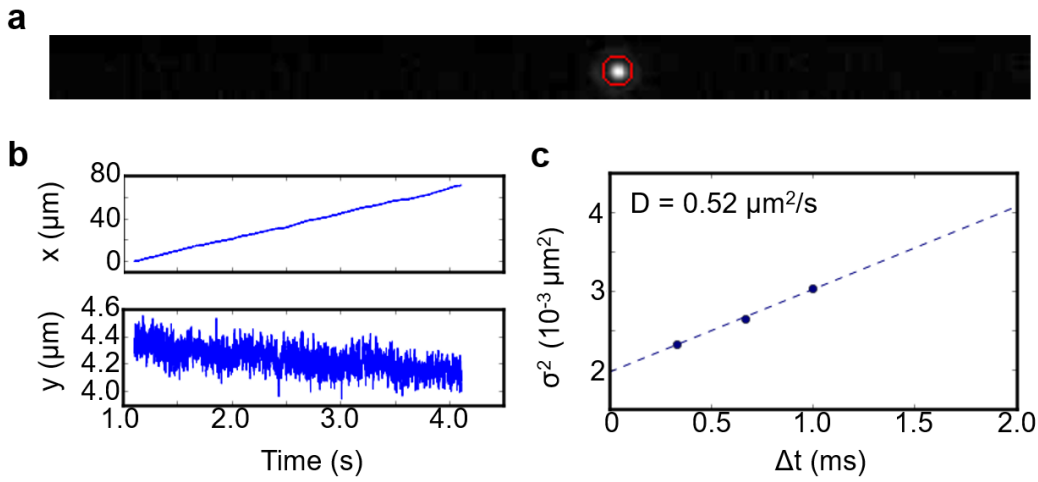

Figure 4.6: Dynamic analysis of a trapped R=150 nm polystyrene bead. a) A still image of the scattered light signal from the trapped particle. The red circle shows the particle location determined by the spot tracking algorithm. b) The 2D trajectory of the particle, captured at 3000 FPS for 3 seconds. The x and y axes are as defined in Fig. 4.1. b) The variance of the particle motion along the y axis as a function of time lag, averaged over the full 3 second trajectory. The effective diffusion coefficient is calculated from a linear fit to the first three points, following the analysis of the simulations in Fig. 4.2.

Brownian dynamics simulations. Along the x-direction, the particle is pushed at a terminal velocity by the balance of the optical scattering force (Eq. 4.3a) and the Stokes drag (Eq. 4.3d), as expected. Along the y-direction, the particle fluctuates about the center of the waveguide, consistent with the Brownian dynamics trajectory generated in Fig. 4.2a. The variance of the displacement was then calculated as a function of the time lag between frames and a linear fit was performed to the first three frame lags (Δt = 1/3000, 2/3000, 3/3000). Using Eq. 4.7, we can then calculate an effective diffusion coefficient of 0.52 $\mu m^2/s$ (Fig. 4.6c).

If we assume the optical power is sufficiently high that the particle is just above

the waveguide surface, we can now apply the result of Eq. 4.10 to estimate the particle size. For this experiment, this approximation works very well and a more refined estimate is not necessary; a measured diffusion coefficient of 0.52 $\mu m^2/s$ corresponds to a particle with radius of 151 nm, less than a 1% deviation from the value of 150 nm quoted by NIST.

For this particle, a full three seconds of data was used to determine the size. The Brownian diffusion along the y-direction is inherently stochastic; as such, there will always be variance in the measured diffusion coefficient, and this variance will depend strongly on the number of frames captured. It is worth investigating, therefore, how well the analysis technique works for shorter trajectories. In Fig. 4.7, we calculate the effective diffusion and radius of the particle for subsets of the full three second video to see the influence of the video length on the final accuracy. For very short trajectories, we see a significant overestimation of the diffusion coefficient (or equivalently, underestimation of the radius.) After one second of data, however, the measured radius is within 10% of the nominal value. For a coarser estimate of size, therefore, it may be possible to characterize a particle in just one second, or 3000 frames of video data. In our previous work, we demonstrated that 3000 frames of data is also sufficient to obtain accurate interaction force measurements, meaning that simultanous measurements of force and size could be achievable in one second with reasonable accuracy. In practice, most dielectric particles remain within the field of view for 3-5 seconds allowing for better convergence and more accurate results [80]. For a concentrated particle solution under ideal conditions, this allows for potential single-particle analysis of around one thousand particles an hour.

For the experimental data here, we have considered only the accuracy of mea-

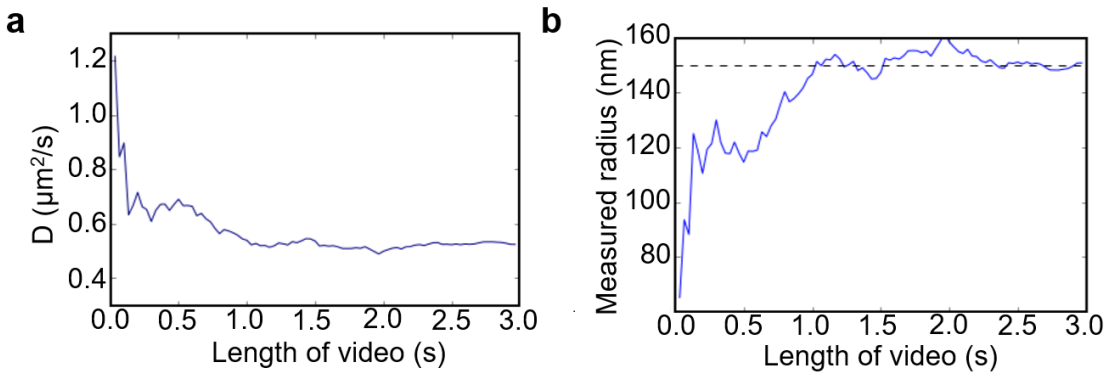

Figure 4.7: Convergence of the measured radius over time. a) The diffusion coefficient is determined by analyzing a subsection of the tracked particle trajectory to determine the length of time required for an accurate value. For short trajectories, the diffusion coefficient is significantly overestimated, but rapidly approaches a final constant value for tracks longer than 1 second. b) The radius calculated from the measured diffusion coefficient using Eq. 4.10. The measured radius shows very good agreement with the nominal radius quoted by the manufacturer (R=150 nm, shown with the dotted line) for times greater than 1 second.

suring a single particle. For very polydisperse samples, however, the reality is slightly more complicated. As discussed previously, the optical gradient force is size dependent (R^3); at a given optical power, larger particles will be held more easily than smaller ones. This in general would lead to a bias in the measured particle distribution, where large particles are overrepresented and small particles are underrepresented.

In the absence of surface forces, this bias can be quantified straightforwardly; a 400 nm particle, for instance, experiences an attractive optical force which is roughly 70% that of a 450 nm particle. The bias is more complicated near the waveguide surface, however, because both the optical gradient forces and the repulsive surface forces increase as the height above the surface decreases. At a

higher optical power, both the larger and smaller particles can be stably held, but will be held at different equilibrium heights. In a high-salt environment with a Debye length of 20 nm, for example, a 7 nm difference in equilibrium height is enough to compensate for the same 30% decrease in optical force strength. Since this effect depends on the magnitude and height-dependence of the surface forces (which are unknown a priori), it cannot be easily estimated from first principles. Because there is simultaneous analysis along multiple axes, however, it should be possible to combine force and size data after an experiment to estimate the degree of bias in the measurement and make appropriate corrections. It would also be possible to directly measure particles at different heights using the multiple powers analysis shown in Fig. 4.4. We hope to investigate this effect in the future by performing experiments with known polydisperse samples, but that is outside the scope of the current work.

While techniques exist to measure both the size and particle-surface interaction potentials of nanoscale particles, there are no existing techniques which can do both simultaneously at high throughput. In this work, we have described an extension to our previous force spectroscopy method which uses the dynamics of a particle within an evanescent field to probe its size, forces, and optical properties. Using a combination of analytic theory and Brownian dynamics simulations, we have outlined the procedure for applying this technique and have investigated the particle sizing accuracy for single particle trajectories. We have also demonstrated the viability of the analysis technique using experimental data gathered under practically realizable conditions, finding very good agreement with the simulated results with only 3 seconds of video data. We believe this technique could be used to process hundreds of particles per hour using a commercial CMOS camera, making it especially viable for rapid quality control of nanoparticle suspensions.

Conflict of interest

The authors declare the following competing financial interest(s): D.E. has an equity interest in Optofluidics, Inc., a company commercializing technologies related to this work.

Acknowledgments

This work was supported by the US National Institutes of Health under grant 1R01GM106420-01. The authors would like to thank Dr. Christopher Earhart from Optofluidics, Inc. for valuable discussions and relevant experimental parameters for the numerical simulations.

CHAPTER 5

3D NANOPHOTONIC FORCE MICROSCOPY – ADDITIONAL THEORY AND EXPERIMENT

5.1 Abstract

In this Chapter, I will extend the theoretical model from the previous chapter to include the motion along the x-direction. I will also show additional experimental data to test the predictions of both the x- and y-direction theory. Here, we have performed experimented on polystyrene beads (R=260 nm and R=400 nm) and gold nanoparticles (R=150 nm), and tracked the nanoparticle transport in all three dimensions by localizing and integrating the scattered light distribution. The x, y and z direction motion are obtained simultaneously for each particle in only a few seconds each and the results of the characterization analysis agree with both the theory from the previous chapter as well as the spread in the particle size distribution quoted by the bead manufacturers.

5.2 Introduction

In the previous chapter, the focus was establishing a mathematical framework for sizing a particle which is trapped above an optical waveguide, and proving this framework with an experimental demonstration.

This work was conducted equally with my colleague Perry Schein who originally developed the force analysis technique for the z-axis and also performed some of the experiments and analysis in this chapter.

Here, we expand on this theory to include analysis of both the x- and y-direction motion of single particles and provide experimental data on a larger body of individual particles. Taking advantage of the optical waveguide architecture to transport nanoparticles in a high-throughput, conveyor-belt style rapid interrogation approach, we track the motion in all three dimensions, and discuss how to extract different orthogonal characterization data from each axis. Using polystyrene particles of known radius (R=260 nm and R=400 nm), we then demonstrate the application of the theory in both x and y on 33 single nanoparticles to develop population statistics. Although there is still room for improvement on each axis, we believe that making simultaneous measurements in three dimensions has significant potential for enabling better high-throughput nanoparticle analysis.

5.3 3D particle tracking

The physical system used in these experiments is a silicon nitride waveguide with a width of 600 nm placed within a microchannel used for delivering nanoparticles to the waveguide surface. (For a detailed schematic of this setup, see Fig. A.3 in Appendix A.) As a nanoparticle interacts with the evanescent field, the various components of the optical forces transport the particle along the waveguide. The dynamics of the nanoparticle motion are complex, and caused by a combination of optical gradient forces (pulling towards the center of the waveguide), optical scattering forces (pushing along the axis of propagation), and stochastic Brownian forces. The x-y motion of the particle can be tracked over time using the techniques of single particle tracking, as in the previous chapter [92].

An additional effect of the particles interaction with the evanescent field is that

the particle scatters light. This scattering depends on the size and refractive index of the particle, but for a given particle over time the amount of light that it scatters corresponds to the local available optical intensity in the evanescent field, which is an exponentially decaying function of the distance above the waveguide. In this way, the fluctuations in the position and the intensity of the scattered light signal over time allow for the particle motion to be tracked in all three spatial dimensions, with each dimension supplying complementary information. This is the basis of the orthogonal measurement methodology that we demonstrate here.

Fig. 5.1 outlines the orthogonal characterization procedure. From a captured image of the scattered light as the nanoparticle interacts with the waveguide, the particle position is localized in each frame, as illustrated by the red circle in Fig. 5.1(a). Based on 2D Gaussian fitting [92] the x and y position of the particle centroid are localized with sub-pixel resolution as shown in Fig. 5.1(b) and 5.1(c) respectively. This information is then used to draw a 12x12 pixel box around the centroid position. All of the pixel values inside this box are added up, giving a value for the total intensity scattered by the particle as shown in Fig. 5.1(d). These values are captured in every frame from a tracked particle, giving the scattering velocity (which will be related to the polydispersity), the y-direction diffusion coefficient (which will be related to the particle size), and the z-direction interaction energy landscape (which can be related to the suspension's stability). Each of these orthogonal measurements will now be discussed separately in the following sections.

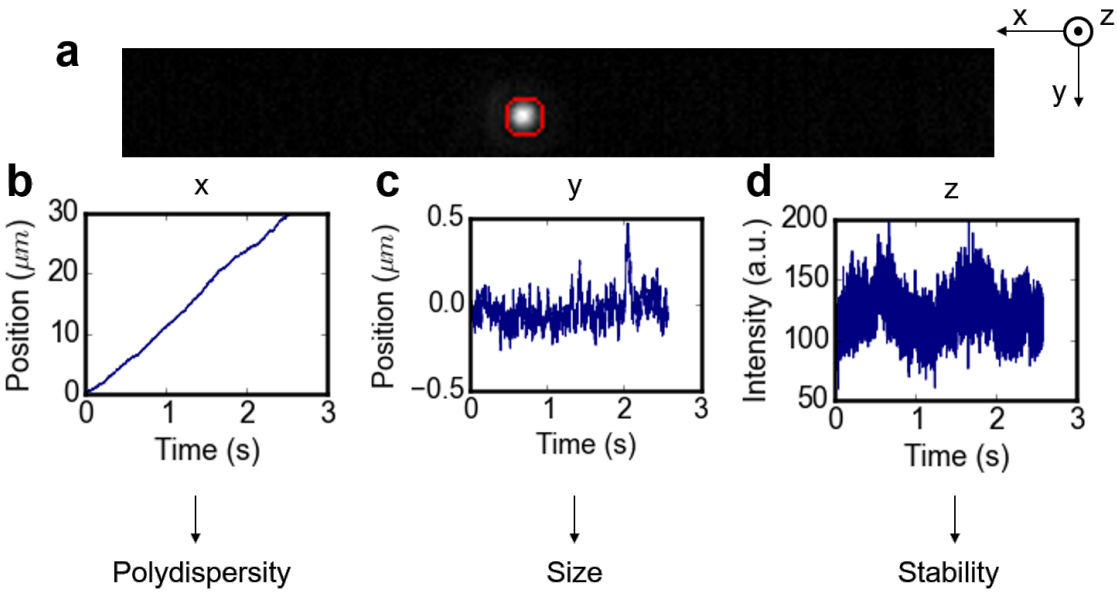

Figure 5.1: Orthogonal nanoparticle characterization scheme. (a) A particle is transported along an optical waveguide, scattering light as it interacts with the evanescent field. This scattered light is captured and recorded using a CMOS camera (example frame shown). The particle position is localized in each frame (red circle).The centroid position of the particle is tracked with sub-pixel resolution and the total intensity of light scattered by the particle is integrated in each frame. (b) In the x-direction (coordinate system shown in the upper-right corner of this figure) the particle translates at a terminal velocity, and the distribution in terminal velocities over the particle population gives a measurement of sample polydispersity. (c) In the y-direction, the particle undergoes confined and hindered diffusion in a harmonic potential well near the surface, which can ultimately be related to the particle size. (d) In the z-direction, the particle scatters more light when it is close to the waveguide and less when it is far away, so the scattered light intensity is used to track the z-position. Over many samples, the statistical distribution of scattered light intensity gives the probability distribution of finding the particle at a given energetic state, corresponding to a height in the potential energy well. Using the Boltzmann distribution, these probabilities give a map of the potential energy landscape, which is related to the energy barrier preventing the particle from sticking to the surface and therefore indicative of the suspension stability.

5.3.1 y-direction – particle size information

In the y-direction, the particle sees a potential energy well due to the optical intensity gradient of the mode profile of the waveguide. For single-mode operation, this will be strongest above the center of the waveguide and decreasing towards the edges. This results in an optical gradient force restoring the particle to the central intensity maxima. For small displacements from the center of the waveguide, these forces can be approximated as being linear in the y-displacement, and the particle experiences a harmonic potential well. For the waveguide geometry used here, the assumption of linearity is valid for displacements that are smaller than ± 100 nm, as can be seen from the mode profile in Fig. A.4. Since the theoretical framework for extracting the diffusion coefficient was developed in our previous work, I will not repeat the full derivation here. As before, we consider only the motion of the particle at short time scales where the variance in the position distribution grows linearly with time:

$$\sigma^2(\Delta t) = 2D\Delta t \tag{5.1}$$

From this, we can find an effective diffusion coefficient $D_{||}$ which is hydrodynamically hindered from the bulk diffusion value by a height-dependent factor β such that:

$$D_{||} = \beta(z, R) D_{bulk} \tag{5.2}$$

As z approaches 0, this factor β reduces to 0.324 for all values of R, but it is in general a complex, nonlinear function of R.

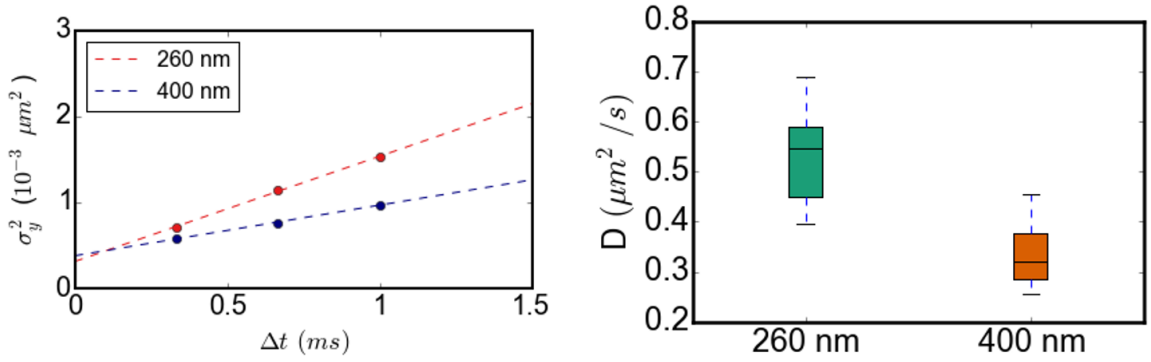

Figure 5.2: Analysis of y-direction motion. (a) Variance in y-position as a function of lag time for example R = 260 nm (red curve) and R = 400 nm (blue curve) nominal sized particles (only short lag times shown). At short times the particle does not yet have time to respond to the restoring forces, and the transport occurs as it would in the absence of the optical trap. Linear fits are shown with dashed lines. The slope of these lines corresponds to the diffusion coefficient. (b) Population level measurements of diffusion coefficient. The smaller diameter particles diffuse faster, allowing for the two particle populations to be distinguished.

To demonstrate this technique for particles of different sizes, we performed two experiments: one using R = 260 nm polystyrene beads and the other R = 400 nm polystyrene beads. The results of these experiments are shown in Figure 2. In Figure 2(a), the short time data is plotted for one particle of each size. As expected, the variance in the 260 nm particle motion increases more rapidly than the 400 nm one, consistent with higher diffusion (and therefore a smaller particle). Figure 2(b) shows a boxplot with aggregated effective diffusion coefficients from all particles measured. N = 8 particles are plotted for the 260 nm set, and N = 25 for the 400 nm set.

If we compare the mean value of the diffusion coefficient for the two data sets, the 260 nm beads are indeed distinguishable from the 400 nm beads by their effective diffusion coefficient. If we take the approximation that , however, we find

a measured radius of 149 nm and 238 nm, respectively 60% of the nominal radius for both particles. There are a number of possible explanations for this bias– for example, that the equilibrium position of the particle is significantly above the surface, rendering the z=0 approximation invalid, or that there are other sources of apparent particle movement in addition to the real diffusion, e.g. vibrations in the microscope setup. The bias is not likely attributable to under-sampling the particle motion in the presence of the force-field, as this would result in an underestimate of the diffusion coefficient (and thus an overestimate of the particle size). Additional experiments must be conducted to determine the origin of the bias, but the two particle populations are still separable from one another by size even with this bias present.

5.3.2 x-direction – polydispersity

The y-direction analysis is valuable because it yields a hydrodynamic estimate of particle size, which is independent of the particle's optical properties or the optical power used. Unfortunately, this is a stochastic estimator, and there is a lower bound on the variance in size estimate. As such, it can be useful for distinguishing 300 nm particles from 600 nm particles, but cannot resolve small deviations, e.g. 300 nm particles from 305 nm. These small differences in size can, however, be very significant for determining the reliability of the particle distribution. To determine this spread in the particle size distribution, we can add an additional orthogonal measurement from the x-direction motion.

In the x-direction, the optical scattering and absorption forces are balanced by the hydrodynamic drag on the particle, which travels at a terminal velocity with some fluctuations due to changes in the optical forces resulting from the

coupled motions in the other directions, as well as due to Brownian motion in the x-direction itself.

For a dielectric Rayleigh particle, the optical absorption forces are negligible, and we can consider only the balance of the scattering and drag forces:

$$F_{scat} = \frac{128\pi^5 I_0 \epsilon_m}{3c\lambda^4} \left(\frac{\epsilon_p - \epsilon_m}{\epsilon_m + 2\epsilon_m} \right)^2 R^6 \tag{5.3a}$$

$$F_{drag} = 6\pi\eta R U_0 \tag{5.3b}$$

where I is the locally available optical intensity in the evanescent field, ϵ_m is the relative permittivity of the medium, ϵ_p is the relative permittivity of the particle, c is the speed of light in vacuum, λ is the optical wavelength, η is the viscosity of the medium, U_0 is the velocity along the x-direction, and R is the particle radius.

Combining the two, we can derive an expression for this terminal velocity:

$$U_0 = \frac{64\pi^4 I_0 \epsilon_m}{9c\lambda^4 \eta} \left(\frac{\epsilon_p - \epsilon_m}{\epsilon_m + 2\epsilon_m} \right)^2 R^5 \tag{5.4}$$

This velocity is very strongly dependent (R^5) on the particle size, so small differences in the particle size can yield easily measurable differences in the measured velocity. The prefactor in Equation 5.4 is in general unknown so the radius cannot be found directly from the velocity. If a solution of multiple nanoparticles are measured under the same experimental conditions, e.g., on the same waveguide and at the same optical power, however, the velocity of two particles can be directly compared to find the difference in radius:

$$\Delta R = R\left[\left(\frac{U_{0,R+\Delta R)}}{U_{0,mean}}\right)^{1/5} - 1\right] \tag{5.5}$$

where $U_{0,mean}$ is the mean velocity of all the particles, R is the mean radius of the particles (from either the manufacturer's specifications or the y-direction motion), and $U_{0,R+\Delta R}$ is the velocity of an individual measured particle. If a statistically significant number of particles are processed, this gives a highly sensitive measurement of the variance in the particle size within the sample. Combined with the mean radius, it is also possible to calculate the coefficient of variation of the nanoparticle distribution, a useful quality control metric to quantify polydispersity within the distribution.

Fig. 5.3 shows this x-direction analysis for the same particles as in Fig. 5.2. As each particle is transported along the waveguide, it rapidly reaches a terminal velocity. Because the x-direction motion is steady and ballistic, the error in determining the velocity is much lower than the stochastic uncertainty from the y-direction motion. By comparing the velocity of each trajectory to the average velocity for the full dataset, we can apply Equation 5.5 to find differences in the particle size to single nanometer precision. We can then use these variations to compute the standard deviation in particle radius, which when divided by the nominal sample radius supplied by the manufacturer gives us the coefficient of variation (CV). For the nominal R=400 nm particles, the variance is found to be ± 5 nm, yielding a coefficient of variation of 0.5%. This agrees well with the CV of 0.6% and radius 4.5 nm specified on the Certificate of Analysis from the manufacturer, as measured by Transmission Electron Microscopy.

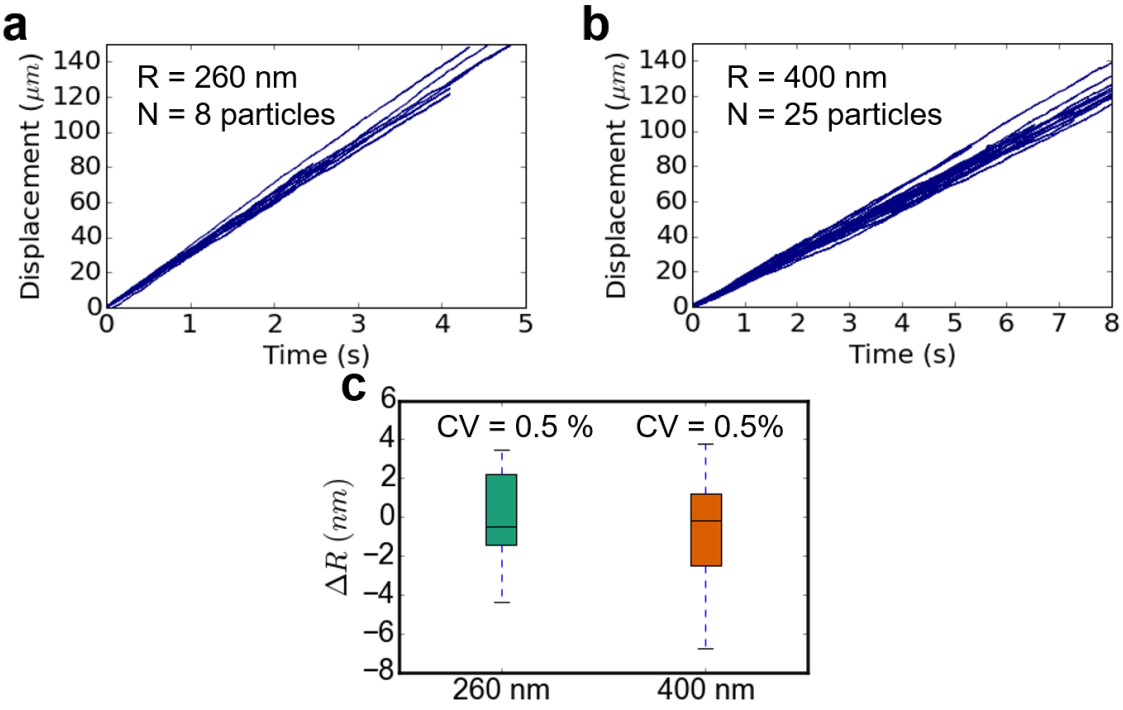

Figure 5.3: Analysis of x-direction motion. Top: x-position traces for (a) R = 260 nm and (b) R = 400 nm particles. The particles reach terminal velocity far faster than the timescale of these measurements. As the velocity depends on R^5, the spread in the terminal velocity (spread in the slopes) is related to the sample polydispersity. (c) Spread in particle radii (ΔR) for 260 nm and 400 nm samples. The coefficient of variation calculated with our methodology is consistent with the values certified by the manufacturer as determined through TEM.

5.3.3 z-direction – solution stability

In addition to the motion in the x-y plane, the nanoparticles also experience forces and resulting motion normal to the surface in the z-direction. Unlike the x-y measurements that track the centroid position of the particle, the z-direction motion is tracked by integrating the total intensity scattered by the particle when the particle is near the surface, the evanescent field intensity is stronger so the par-

ticle scatters more light and a brighter signal is observed. From the z-direction motion, it is possible to directly measure the forces between the nanoparticle and the waveguide surface. This analysis is outside the scope of this chapter, but has been well established by our previous work for particles in this size regime. The interested reader is directed to two of our previous studies for further details on the method and practical demonstrations [80, 81].

5.4 Discussion

Currently, our estimates of size from the y-direction diffusion suffer from relatively large uncertainties which make it difficult to discern small differences in the size. Because confined Brownian motion is a stochastic process, there will always be a degree of variance in the measured diffusion coefficient. The lower bound on this uncertainty will improve with more frames, however, as would any systematic biases in the measured size due to undersampling the diffusive motion. As a result, the accuracy of this technique can be improved significantly by observing the motion with a faster camera. Given the rapid progress in camera quality and data transfer rates in recent years, we predict that it will soon be possible to greatly improve the uncertainties of the sizing technique without switching to expensive, specialized equipment.

The x-direction analysis gives results that are consistent with the manufacturers specification for these particles. This has significant potential as a rapid measure of the variance in the particle size distribution, especially because it can be added to our existing techniques with no additional experimental or computational overhead. However, the analysis presented in Fig. 3 depends on the

particle having a well-defined terminal velocity. For much smaller nanoparticles, the forward scattering force will not be large enough relative to the particle's diffusion, and fluctuations in the particle motion along the x-direction will limit the accuracy of the measurement. For this reason, we estimate that the combined orthogonal technique as described here is limited to particles roughly R=100-150 nm and larger. Fortunately, the technique does cover a large part of the so-called subvisible regime of 100 nm to 10 μm where existing techniques are considered insufficient for high-throughput characterization, and therefore may be a valuable addition to the current toolbox [5, 6].

5.5 Conclusions

Here, we have demonstrated the viability of making orthogonal measurements by tracking the motion of the nanoparticle in multiple spatial dimensions. We have performed proof of concept experiments on NIST-traceable nanoparticle suspensions and obtained results that in line with expectations. Measurements of the y-direction diffusion show that particles of different sizes can be distinguished, while velocity measurements in the x-direction are used to calculate the coefficient of variation of the particle size distribution. This technique can be used to gain quantitative information about nanoparticle populations as well as identify possible outliers within a solution in terms of size or chemical composition.

CHAPTER 6

CONCLUSIONS AND FUTURE DIRECTIONS

6.1 Directed self-assembly and binding

In Chapters 2 and 3 of this dissertation, I have laid out two sets of experiments using optical forces for controlling both inorganic and biological binding interactions. I believe these experiments serve as a solid proof-of-concept that optical forces have unrealized potential for precision control and assembly. Unfortunately, the implementation used for this demonstration does not scale well and is too impractical for realistic self-assembly. There are two principal reasons for this: the first is that the assembly process here is irreversible and requires cleaning of the waveguide chip in between experiments, and the second is that we have limited control apart from the intrinsic mode shape of the carbon nanotube mode profile.

Building on the results, one approach to improve the tunability of the hybrid optical resonators and enable more control is to fabricate the plasmonic resonators instead of assembling them directly on-chip. There have been some recent designs which integrate nanofabricated gold nanoantennas directly onto an optical waveguide [93,94]. In this setup, the exact mode profile of the resonator can be predicted with nanometer precision and multiple resonators can be fabricated into a pattern to produce more interesting geometries. A more ambitious approach would be to use a full 2D structure, for instance a 2D photonic crystal [95], a 2D array of plasmonic resonators [96], or a hybrid design combining both elements, as in a recent theoretical work by Mossayebi et al. [97]. With one of these architectures, it would be possible to achieve much greater trapping forces and also assemble nanoparticles into 2D shapes using a pre-designed or modular mode shape. If this is done

without irreversible sticking to the resonator surface, the potential throughput here could be orders of magnitude higher than the results presented in this dissertation. There will be significant engineering and technical challenges, however, that must first be addressed before this can be truly viable as a scalable synthesis method.

6.2 Nanoparticle characterization

Chapters 4 and 5 describe both theoretical and experimental work on an nanoparticle characterization technique. We have shown that by tracking the motion of a single nanoparticle as it moves through a complex (but well-understood) nonuniform optical field, it is possible to extract a large amount of information about the particle's properties, including its size, refractive index, and interactions with the waveguide surface. There are a few key areas where additional research could be very beneficial.

6.2.1 Improving the experimental setup

A significant effort was made to improve throughput and viability in real-world quality control situations and the current technique is achievable with a setup that is commercially available now with a low-cost camera. This decision was made to help fill a gap in high-throughput characterization techniques in the so-called sub-visible range of particles between 100 nm and 10 microns [5,6]. Nevertheless, there are some disadvantages to this setup. Using the current industrial camera, the maximum practically achievable frame rate is around 3000 FPS. This is sufficient to resolve diffusive motion along the y-direction, but not along the z-direction.

With a faster frame rate, there would be significantly more frames along y (improving the accuracy of the stochastic analysis) and also the potential to measure the hindered diffusion along z. Since the diffusion along z has a different dependence on height than the in-plane diffusion [88], the combination of the two can uniquely specify the size even for particles where the h=0 assumption does not hold. Given the steady and rapid progress of CMOS camera technology, this may well be possible with a low-cost experimental setup in the near future.

6.2.2 Surface functionalization

A key advantage of the demonstrated technique is the ability to probe the interactions of particles and the waveguide surface. With the current design, however, all of these forces are relative to a silicon nitride surface, which is of limited utility. One way to probe more relevant surface interactions is to functionalize the waveguide surface with a material that approximates a surface of significance in a real-world application. This could take the form of chemical surface groups, deposited metallic layers, or even a self-assembled lipid layer for biophysical investigations. If the same particles can be analyzed on multiple waveguides with different surface materials, it would be a useful way of directly investigating fundamental colloid interactions or biophysical (e.g. protein-protein) interactions which are difficult to predict with current theories. A schematic of this proposed experiment is included in Fig. 6.1.

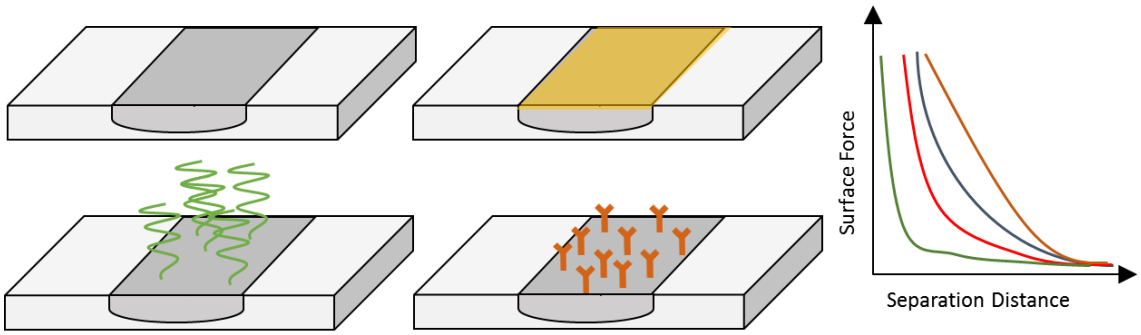

Figure 6.1: Schematic overview of a proposed experiment. By functionalizing the waveguide surface with different materials (both organic and inorganic), it may be possible to experimentally predict the behavior of a given nanoparticle in different physically relevant situations. The hypothetical surfaces here are a bare waveguide, a deposited gold monolayer, an inorganic polymer layer, and a layer of polyclonal antibodies.

6.2.3 Protein aggregate analysis

In terms of potential applications, there are a multitude of scientific fields and industries that could benefit immensely from better nanoparticle characterization techniques. One of the most intriguing, I think, is the detection of protein aggregates in solutions of protein therapeutics. There is a growing body of evidence that aggregated therapeutic proteins can have many deleterious side effects, including life-threatening anaphylaxis [5]. Unfortunately, protein aggregates are very difficult to quantify because they come in a wide variety of sizes and conformations, and can form at any stage of the drug production pipeline. There is a pressing need, therefore, for a technique that can detect and analyze nanoscale protein aggregates. I believe the characterization technique shown here has potential to address this need, because it can give both a rough estimate of size (which for aggregates is unknown) and a measure of surface interactions (which, for a suitable surface, might be used to predict the aggregate's conformation or its behavior dur-

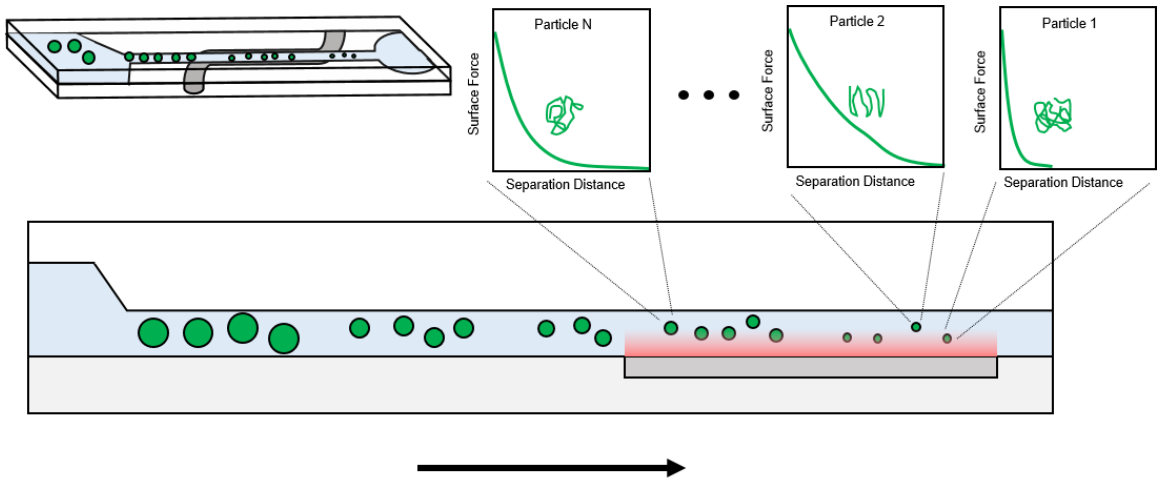

Figure 6.2: Schematic overview of a proposed protein aggregate characterization device. As each of the protein aggregates passes over the waveguide, it is tracked in three dimensions to estimate the size and surface forces. By combining these two data points, a histogram can be built up of the number of aggregates with a given conformation in each size range. This data has potential to greatly improve our understanding of how many aggregates are present and what effects they are likely to have.

ing drug production, storage, or injection). A schematic of a hypothetical protein analysis assay is shown in Fig. 6.2.

To demonstrate this, Fig. 6.3 shows a preliminary experiment trapping a thermal aggregate of bovine serum albumin (BSA). Both the effective diffusion coefficient and the particle-surface forces can be calculated from its motion. The predicted size for this aggregate, assuming the particle is near the surface, is R=70 nm but the accuracy of these results is hard to quantify as the actual size is unknown. Additional work with protein aggregates, particularly with carefully controlled manufacturing of aggregates of known size and conformation, could be invaluable for the development of a reliable nanoscale aggregate characterization technique.

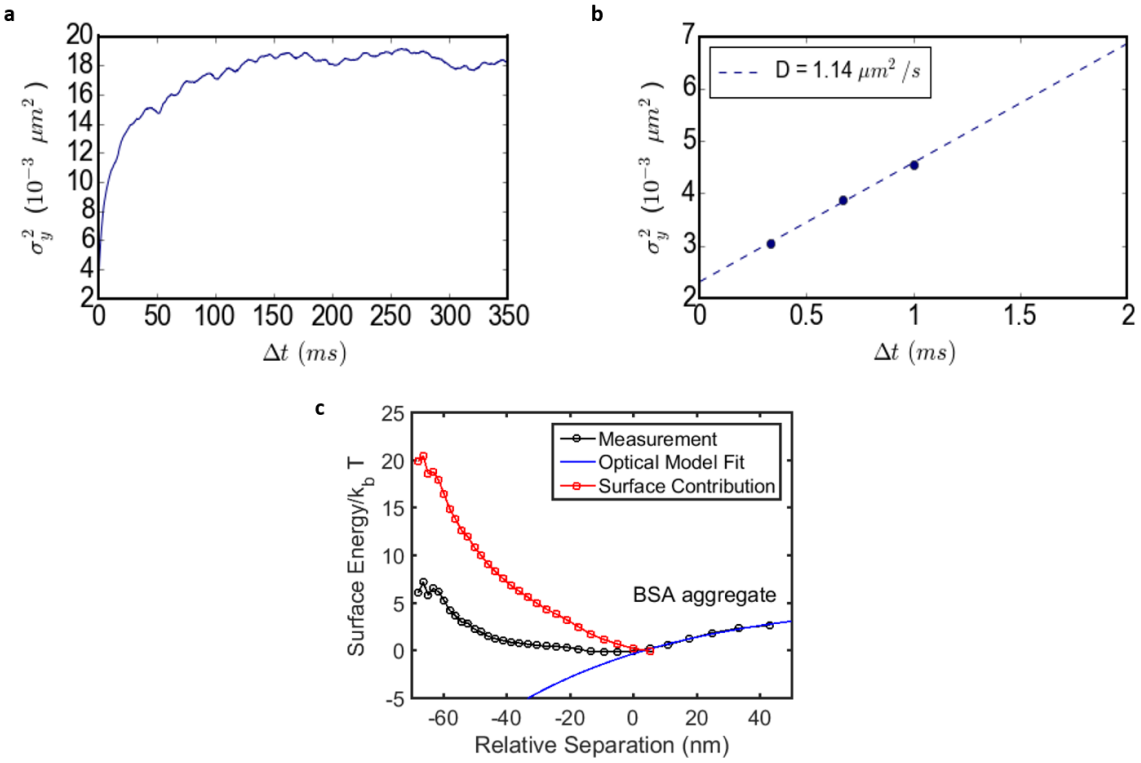

Figure 6.3: Preliminary data on protein aggregate characterization for thermally-aggregated BSA. a) The variance in the y-direction motion as a function of time lag. b) From the short time data, we find a diffusion coefficient of 1.14 $\mu m^2/s$. Using the near-surface approximation, this yields a particle radius of 70 nm. c) The particle-surface interaction potential well calculated for the BSA aggregate, courtesy of Perry Schein.

APPENDIX A

SUPPLEMENTAL DISCUSSION AND FIGURES

A limitation of plasmonic optical trapping is that ohmic losses in the metallic structures can generate a lot of heat in the surrounding medium. This heat will increase the local temperature near the surface, which can lead to thermal forces and convective flows. Here, we discuss potential thermal effects which might influence the adsorption reaction, as well as control experiments to determine the relative importance of thermal and opto-mechanical forces. These thermal mechanisms come in two types:

(1), effects dependent on T, such as the temperature dependence of the Boltzmann factor governing the binding reaction, and (2), effects dependent on , such as thermophoresis and electrothermally-induced flow. We address both classes separately.

(1) To discount effects which depend on the magnitude of the local temperature, we performed a control experiment in which we heat the fluid an additional 60 K above ambient using a hot plate. This is higher than the temperature near the CNT during observed adsorption events at high salts. If the temperature dependence of the reaction kinetics, e.g., was a dominant factor, this should be enough to adsorb proteins without optical power. Since we do not observe this even over several hours, high temperature alone is not sufficient.

(2) There are also thermal effects which depend on a temperature gradient. Even if the bulk temperature is increased globally for a control experiment, there can still be a significant local temperature increase near the nanotube due to Joule heating. In the DLVO model developed here, we have accounted for the ther-

mophoretic force which was negligible compared with the optical component. An additional force which is not included in the model is the electrothermal effect, in which a temperature gradient leads to a gradient in the local electrical conductivity and permittivity, and generates a body force on the fluid. This force is given by

$$f_{ET} = -\frac{1}{2}\left[\left(\frac{1}{\sigma_m}\frac{\partial \sigma_m}{\partial T} - \frac{1}{\epsilon_m}\frac{\partial \epsilon_m}{\partial T}\right)\nabla T \cdot E\frac{\epsilon_m E}{1+(\omega\tau)^2} + \frac{1}{2}|E|^2\frac{\partial \epsilon_m}{\partial T}\nabla T\right] \qquad \text{(A.1)}$$

where ω is the frequency of the electric field, and $\tau = \epsilon_m/\sigma_m$ is the charge relaxation time of the medium [98, 99]. Although this first term can generate strong flows towards an electrode at low frequencies, the Coulomb forces will be negligible at optical frequencies where $\omega >> 1/\tau$ and the charges do not have time to accumulate. In this limit, electrothermal flow will be significantly weaker and also away from regions of high temperature, meaning that it may be a second-order effect on the measured power threshold, but is not the driving force behind the adsorption reaction.

In recent work, Ndukaife et al. have demonstrated that attractive electrothermal flow is possible with light-induced heating from a 1064 nm laser if a lower frequency AC electric field is applied. When the electrode is turned off, however, the strong attractive force disappears. This observation is consistent with our calculations and further suggests that the thermal forces in our experiments are insufficient to drive the trapping or adsorption of proteins at optical frequencies.

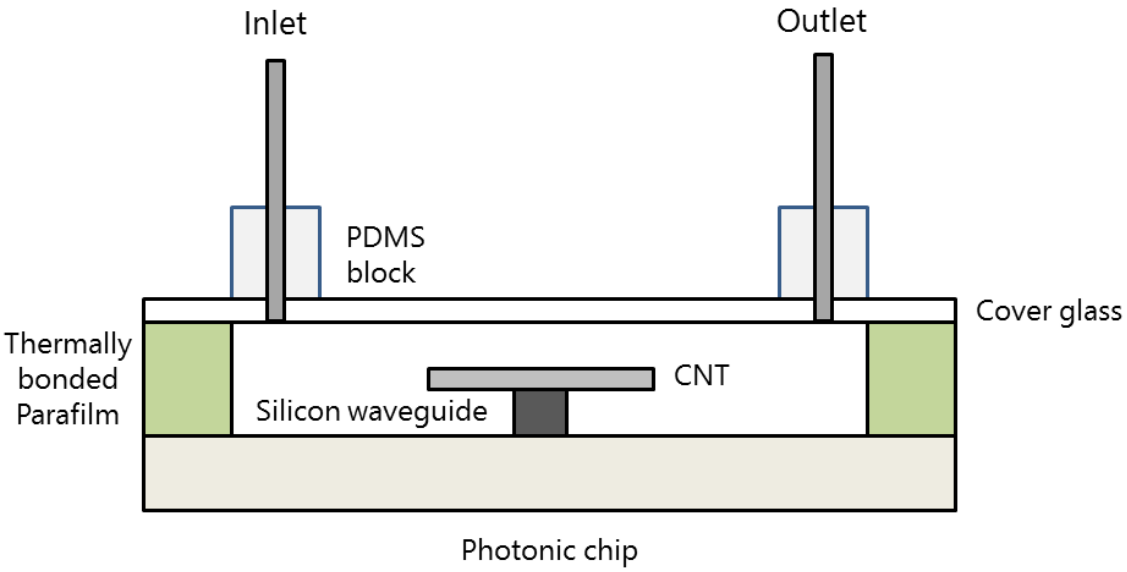

Figure A.1: A schematic overview of the microfluidic setup. A rectangular cavity is cut out of a piece of parafilm using a laser cutter to form the microfluidic channel. A millimeter sized hole is drilled in both sides of a glass cover slide to allow for inlet and outlet tubing, and the glass is thermally bonded to chip with the parafilm layer. A PDMS block is bonded over the inlet and outlet holes using irreversible oxygen plasma bonding to hold the inlet and outlet tubing. Because of this channel geometry, it is possible to image through standard microscope glass instead of a thicker polymer layer (e.g., PDMS), allowing for high-resolution imaging of both the fluorescence emission and infrared laser light.

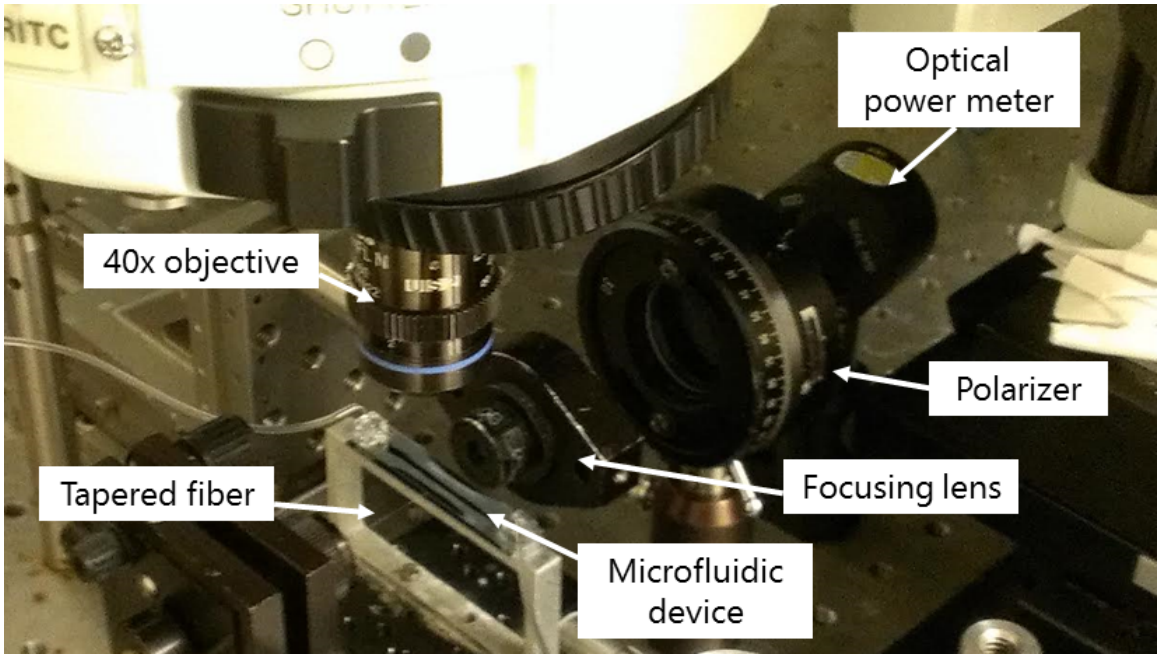

Figure A.2: Schematic of the optical intensity surrounding an arbitrary plasmonic rod on resonance, fed by an optical waveguide. The optomechanical force is proportional to the gradient in intensity, and pulls dielectric particles along the gradient towards the surface. The highest optical gradient is near the ends of rod, but there can also be secondary higher-order hotspots along the rod which will also enhance the optical force. The intensity profile for the nanotubes used in these experiments will vary depending on the nanotube geometry and orientation, but the dielectric gradient force is always attractive towards the surface and can counterbalance the repulsive electrostatic forces.

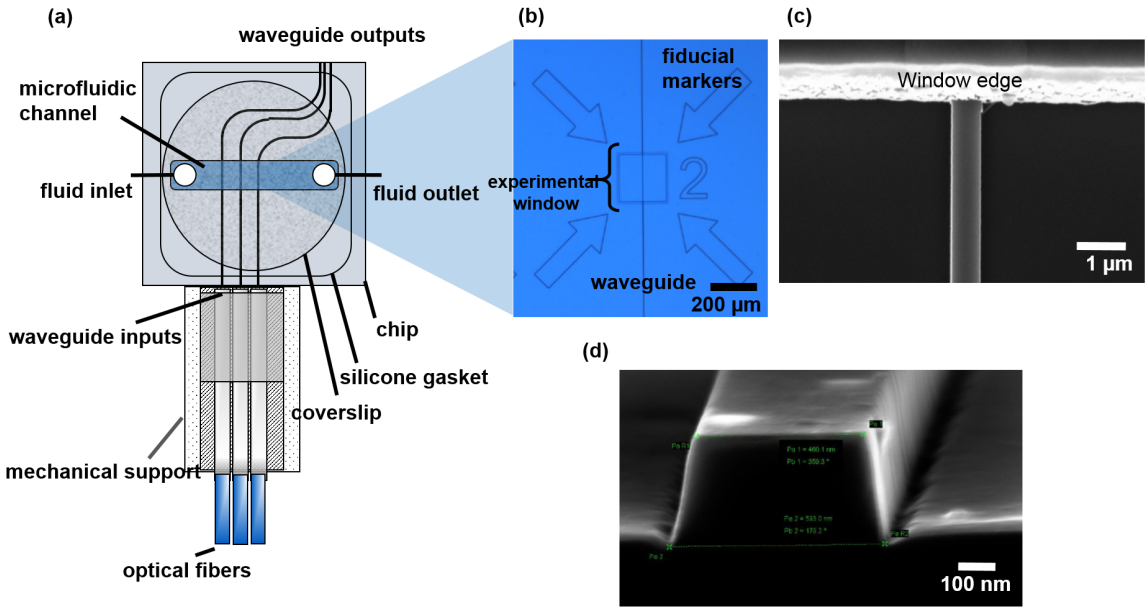

Figure A.3: NanoTweezer chip design. (a) Each chip consists of three waveguides, a microfluidic channel, and an optical fiber assembly for waveguide excitation. The waveguides are cladded by glass across the entire chip with the exception of the experimental window (b), in which a sample delivered to the microfluidic channel interacts with the waveguide. (c) SEM micrograph showing edge of experimental window. (d) Cross-sectional view of waveguide structure. Figure reproduced from [80]

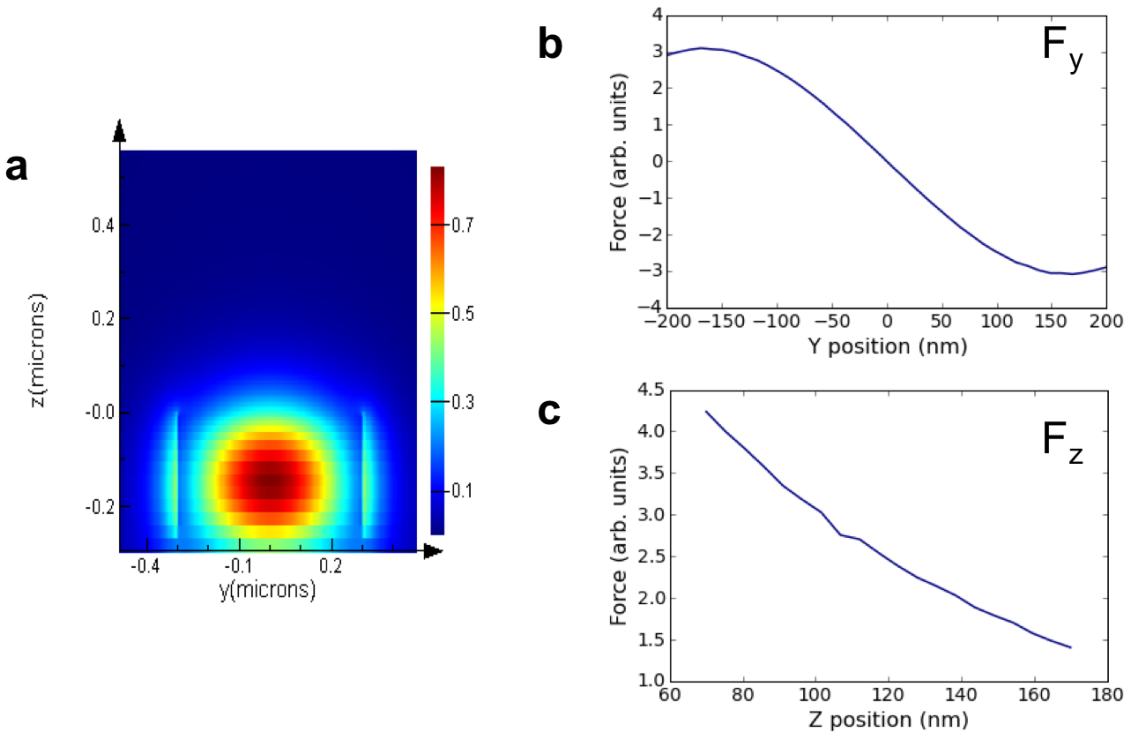

Figure A.4: Finite difference time domain simulations of the waveguide in Fig. A.3. (a) Optical intensity in and around the waveguide (plotted in arbitrary units). (b) The y-direction component of the optical gradient force. Although the force is not strictly linear with displacement, the harmonic approximation remains valid for displacements of at least ± 100 nm. (c) The z-direction component of the optical gradient force. The magnitude of this force decreases exponentially with increasing height above the surface.

BIBLIOGRAPHY

[1] Rajesh Singh and James W Lillard. Nanoparticle-based targeted drug delivery. *Experimental and molecular pathology*, 86(3):215–223, 2009.

[2] Masatake Haruta. When gold is not noble: catalysis by nanoparticles. *The chemical record*, 3(2):75–87, 2003.

[3] Xiliang Luo, Aoife Morrin, Anthony J Killard, and Malcolm R Smyth. Application of nanoparticles in electrochemical sensors and biosensors. *Electroanalysis*, 18(4):319–326, 2006.

[4] Brian R Saunders and Michael L Turner. Nanoparticle–polymer photovoltaic cells. *Advances in colloid and interface science*, 138(1):1–23, 2008.

[5] John F Carpenter, Theodore W Randolph, WIM Jiskoot, Daan JA Crommelin, C Russell Middaugh, Gerhard Winter, Ying-Xin Fan, Susan Kirshner, Daniela Verthelyi, Steven Kozlowski, et al. Overlooking subvisible particles in therapeutic protein products: gaps that may compromise product quality. *Journal of pharmaceutical sciences*, 98(4):1201–1205, 2009.

[6] Thomas M Scherer, Stephenie Leung, Laura Owyang, and Steven J Shire. Issues and challenges of subvisible and submicron particulate analysis in protein solutions. *The AAPS journal*, 14(2):236–243, 2012.

[7] Marie Gaumet, Angelica Vargas, Robert Gurny, and Florence Delie. Nanoparticles for drug delivery: the need for precision in reporting particle size parameters. *European journal of pharmaceutics and biopharmaceutics*, 69(1):1–9, 2008.

[8] Rudolf Merkel. Force spectroscopy on single passive biomolecules and single biomolecular bonds. *Physics Reports*, 346(5):343–385, 2001.

[9] Jens-Christian Meiners and Stephen R Quake. Femtonewton force spectroscopy of single extended dna molecules. *Physical Review Letters*, 84(21):5014, 2000.

[10] M. Bostrom, D. R. M. Williams, and B. W. Ninham. Specific ion effects: Why dlvo theory fails for biology and colloid systems. *Physical Review Letters*, 87(16):168103, 2001.

[11] A. Ashkin, J. M. Dziedzic, J. E. Bjorkholm, and Steven Chu. Observation of a single-beam gradient force optical trap for dielectric particles. *Optics Letters*, 11(5):288–290, 1986.

[12] Tobias J. Kippenberg and Kerry J. Vahala. Cavity opto-mechanics. *Optics Express*, 15(25):17172–17205, 2007.

[13] Jeffrey R. Moffitt, Yann R. Chemla, Steven B. Smith, and Carlos Bustamante. Recent advances in optical tweezers. *Annual Review of Biochemistry*, 77(1):205–228, 2008.

[14] A Ashkin and JM Dziedzic. Optical trapping and manipulation of viruses and bacteria. *Science*, 235(4795):1517–1520, 1987.

[15] Satoshi Kawata and Tadao Sugiura. Movement of micrometer-sized particles in the evanescent field of a laser beam. *Optics Letters*, 17(11):772–774, 1992.

[16] Sudeep Mandal, Xavier Serey, and David Erickson. Nanomanipulation using silicon photonic crystal resonators. *Nano Letters*, 10(1):99–104, 2009.

[17] Adel Rahmani and Patrick C Chaumet. Optical trapping near a photonic crystal. *Optics Express*, 14(13):6353–6358, 2006.

[18] Allen H. J. Yang and David Erickson. Optofluidic ring resonator switch for optical particle transport. *Lab on a Chip*, 10(6):769–774, 2010.

[19] Allen H. J. Yang, Sean D. Moore, Bradley S. Schmidt, Matthew Klug, Michal Lipson, and David Erickson. Optical manipulation of nanoparticles and biomolecules in sub-wavelength slot waveguides. *Nature*, 457(7225):71–75, 2009.

[20] Kai Wang and Kenneth B Crozier. Plasmonic trapping with a gold nanopillar. *ChemPhysChem*, 13(11):2639–2648, 2012.

[21] Brian J. Roxworthy, Kaspar D. Ko, Anil Kumar, Kin Hung Fung, Edmond K. C. Chow, Gang Logan Liu, Nicholas X. Fang, and Kimani C. Toussaint. Application of plasmonic bowtie nanoantenna arrays for optical trapping, stacking, and sorting. *Nano Letters*, 12(2):796–801, 2011.

[22] Maysamreza Chamanzar and Ali Adibi. Hybrid nanoplasmonic-photonic resonators for efficient coupling of light to single plasmonic nanoresonators. *Optics Express*, 19(22):22292–22304, 2011.

[23] Hongjie Dai. Carbon nanotubes: synthesis, integration, and properties. *Accounts of Chemical Research*, 35(12):1035–1044, 2002.

[24] M. F. Lin, D. S. Chuu, and K. W. K. Shung. Low-frequency plasmons in metallic carbon nanotubes. *Physical Review B*, 56(3):1430–1439, 1997.

[25] H Kataura, Y Kumazawa, Y Maniwa, I Umezu, S Suzuki, Yo Ohtsuka, and Y Achiba. Optical properties of single-wall carbon nanotubes. *Synthetic Metals*, 103(1):2555–2558, 1999.

[26] Pilgyu Kang, Xavier Serey, Yih-Fan Chen, and David Erickson. Angular orientation of nanorods using nanophotonic tweezers. *Nano Letters*, 12(12):6400–6407, 2012.

[27] Andre E. Nel, Lutz Madler, Darrell Velegol, Tian Xia, Eric M. V. Hoek, Ponisseril Somasundaran, Fred Klaessig, Vince Castranova, and Mike Thompson. Understanding biophysicochemical interactions at the nano-bio interface. *Nat Mater*, 8(7):543–557, 2009.

[28] Gregory G Wildgoose, Craig E Banks, and Richard G Compton. Metal nanoparticles and related materials supported on carbon nanotubes: methods and applications. *Small*, 2(2):182–193, 2006.

[29] Sabahudin Hrapovic, Ehsan Majid, Yali Liu, Keith Male, and John HT Luong. Metallic nanoparticle-carbon nanotube composites for electrochemical determination of explosive nitroaromatic compounds. *Analytical chemistry*, 78(15):5504–5512, 2006.

[30] Sabahudin Hrapovic, Yali Liu, Keith B Male, and John HT Luong. Electrochemical biosensing platforms using platinum nanoparticles and carbon nanotubes. *Analytical chemistry*, 76(4):1083–1088, 2004.

[31] Martin Konopka, Robert Turansky, Joachim Reichert, Harald Fuchs, Dominik Marx, and Ivan tich. Mechanochemistry and thermochemistry are different: Stress-induced strengthening of chemical bonds. *Physical Review Letters*, 100(11):115503, 2008.

[32] L Takacs. Mechanochemistry and the other branches of chemistry: Similarities and differences. *Acta Physica Polonica, A.*, 121(3), 2012.

[33] K Eric Drexler. Nanosystems- molecular machinery, manufacturing, and computation(book). *New York, NY: John Wiley & Sons, Inc, 1992.*, 1992.

[34] Ib Chorkendorff and Johannes W Niemantsverdriet. *Concepts of modern catalysis and kinetics*. Wiley-Vch, 2006.

[35] Richard I Masel. *Chemical kinetics and catalysis*. Wiley-Interscience New York, 2001.

[36] Charles R Hickenboth, Jeffrey S Moore, Scott R White, Nancy R Sottos, Jerome Baudry, and Scott R Wilson. Biasing reaction pathways with mechanical force. *Nature*, 446(7134):423–427, 2007.

[37] Kevin D Ausman, Henry W Rohrs, MinFeng Yu, and Rodney S Ruoff. Nanostressing and mechanochemistry. *Nanotechnology*, 10(3):258, 1999.

[38] K. S. Venkataraman and K. S. Narayanan. Energetics of collision between grinding media in ball mills and mechanochemical effects. *Powder Technology*, 96(3):190–201, 1998.

[39] Mark C Williams and Ioulia Rouzina. Force spectroscopy of single dna and rna molecules. *Current opinion in structural biology*, 12(3):330–336, 2002.

[40] Ross Rounsevell, Julia R. Forman, and Jane Clarke. Atomic force microscopy: mechanical unfolding of proteins. *Methods*, 34(1):100–111, 2004.

[41] M. A. Fox and M. T. Dulay. Heterogenous photocatalysis. *Chemical Reviews*, 93(1):341–357, 1993.

[42] P. Christopher, H. L. Xin, and S. Linic. Visible-light-enhanced catalytic oxidation reactions on plasmonic silver nanostructures. *Nature Chemistry*, 3(6):467–472, 2011.

[43] Parag B Deotare, Irfan Bulu, Ian W Frank, Qimin Quan, Yinan Zhang, Rob Ilic, and Marko Loncar. All optical reconfiguration of optomechanical filters. *Nature Communications*, 3:846, 2012.

[44] S. M. Block, L. S. B. Goldstein, and B. J. Schnapp. Bead movement by single kinesin molecules studied with optical tweezers. *Nature*, 348(6299):348–352, 1990.

[45] Yuanjie Pang and Reuven Gordon. Optical trapping of a single protein. *Nano Letters*, 12(1):402–406, 2011.

[46] Yih-Fan Chen, Xavier Serey, Rupa Sarkar, Peng Chen, and David Erickson. Controlled photonic manipulation of proteins and other nanomaterials. *Nano Letters*, 12(3):1633–1637, 2012.

[47] Ahmed A Al Balushi, Ana Zehtabi-Oskuie, and Reuven Gordon. Observing single protein binding by optical transmission through a double nanohole aperture in a metal film. *Biomedical optics express*, 4(9):1504–1511, 2013.

[48] Lukas Novotny and Bert Hecht. *Principles of nano-optics*. Cambridge university press, 2006.

[49] Dakota O'Dell, Xavier Serey, and David Erickson. Self-assembled photonic-plasmonic nanotweezers for directed self-assembly of hybrid nanostructures. *Applied Physics Letters*, 104(4):043112–043112–5, 2014.

[50] Jacob Israelachvili and Richard Pashley. The hydrophobic interaction is long range, decaying exponentially with distance. 1982.

[51] Kungang Li and Yongsheng Chen. Evaluation of dlvo interaction between a sphere and a cylinder. *Colloids and Surfaces A: Physicochemical and Engineering Aspects*, 2012.

[52] Xavier Serey, Sudeep Mandal, Yih-Fan Chen, and David Erickson. Dna transport and delivery in thermal gradients near optofluidic resonators. *Physical Review Letters*, 108(4):048102, 2012.

[53] A. Stafiej and K. Pyrzynska. Adsorption of heavy metal ions with carbon nanotubes. *Separation and Purification Technology*, 58(1):49–52, 2007.

[54] Robin J Shannon, Mark A Blitz, Andrew Goddard, and Dwayne E Heard. Accelerated chemistry in the reaction between the hydroxyl radical and methanol at interstellar temperatures facilitated by tunnelling. *Nature Chemistry*, 2013.

[55] BW Ninham. On progress in forces since the dlvo theory. *Advances in colloid and interface science*, 83(1):1–17, 1999.

[56] Amrit Kalra, Nihal Tugcu, Steven M Cramer, and Shekhar Garde. Salting-in and salting-out of hydrophobic solutes in aqueous salt solutions. *The Journal of Physical Chemistry B*, 105(27):6380–6386, 2001.

[57] R. Zhang, Y. Zhang, Z. C. Dong, S. Jiang, C. Zhang, L. G. Chen, L. Zhang, Y. Liao, J. Aizpurua, Y. Luo, J. L. Yang, and J. G. Hou. Chemical map-

ping of a single molecule by plasmon-enhanced raman scattering. *Nature*, 498(7452):82–86, 2013.

[58] M. Takase, H. Ajiki, Y. Mizumoto, K. Komeda, M. Nara, H. Nabika, S. Yasuda, H. Ishihara, and K. Murakoshi. Selection-rule breakdown in plasmon-induced electronic excitation of an isolated single-walled carbon nanotube. *Nature Photonics*, 7(7):550–554, 2013.

[59] D. Psaltis, S. R. Quake, and C. H. Yang. Developing optofluidic technology through the fusion of microfluidics and optics. *Nature*, 442(7101):381–386, 2006.

[60] H. Schmidt and A. R. Hawkins. The photonic integration of non-solid media using optofluidics. *Nature Photonics*, 5(10):598–604, 2011.

[61] X. D. Fan and I. M. White. Optofluidic microsystems for chemical and biological analysis. *Nature Photonics*, 5(10):591–597, 2011.

[62] Binshan Ju, Tailiang Fan, and Mingxue Ma. Enhanced oil recovery by flooding with hydrophilic nanoparticles. *China Particuology*, 4(01):41–46, 2006.

[63] Hadi ShamsiJazeyi, Clarence A Miller, Michael S Wong, James M Tour, and Rafael Verduzco. Polymer coated nanoparticles for enhanced oil recovery. *Journal of Applied Polymer Science*, 131(15), 2014.

[64] Satoshi Kokura, Osamu Handa, Tomohisa Takagi, Takeshi Ishikawa, Yuji Naito, and Toshikazu Yoshikawa. Silver nanoparticles as a safe preservative for use in cosmetics. *Nanomedicine: Nanotechnology, Biology and Medicine*, 6(4):570–574, 2010.

[65] Julian A Gallego-Urrea, Jani Tuoriniemi, and Martin Hassellv. Applications of particle-tracking analysis to the determination of size distributions and concentrations of nanoparticles in environmental, biological and food samples. *TrAC Trends in Analytical Chemistry*, 30(3):473–483, 2011.

[66] Yolanda Echegoyen and Cristina Nern. Nanoparticle release from nano-silver antimicrobial food containers. *Food and chemical toxicology*, 62:16–22, 2013.

[67] M Cushen, J Kerry, M Morris, M Cruz-Romero, and E Cummins. Nanotechnologies in the food industryrecent developments, risks and regulation. *Trends in Food Science & Technology*, 24(1):30–46, 2012.

[68] Margriet V. D. Z. Park, Arianne M. Neigh, Jolanda P. Vermeulen, Liset J. J. de la Fonteyne, Henny W. Verharen, Jacob J. Bried, Henk van Loveren, and Wim H. de Jong. The effect of particle size on the cytotoxicity, inflammation, developmental toxicity and genotoxicity of silver nanoparticles. *Biomaterials*, 32(36):9810–9817, 2011.

[69] Carl D. Walkey, Jonathan B. Olsen, Hongbo Guo, Andrew Emili, and Warren C. W. Chan. Nanoparticle size and surface chemistry determine serum protein adsorption and macrophage uptake. *Journal of the American Chemical Society*, 134(4):2139–2147, 2012.

[70] Martin Lundqvist, Johannes Stigler, Giuliano Elia, Iseult Lynch, Tommy Cedervall, and Kenneth A Dawson. Nanoparticle size and surface properties determine the protein corona with possible implications for biological impacts. *Proceedings of the National Academy of Sciences*, 105(38):14265–14270, 2008.

[71] Stefan Tenzer, Dominic Docter, Susanne Rosfa, Alexandra Wlodarski, Jrg Kuharev, Alexander Rekik, Shirley K. Knauer, Christoph Bantz, Thomas Nawroth, Carolin Bier, Jarinratn Sirirattanapan, Wolf Mann, Lennart Treuel, Reinhard Zellner, Michael Maskos, Hansjrg Schild, and Roland H. Stauber. Nanoparticle size is a critical physicochemical determinant of the human blood plasma corona: A comprehensive quantitative proteomic analysis. *ACS Nano*, 5(9):7155–7167, 2011.

[72] S. A. Wissing and R. H. Mller. Solid lipid nanoparticles as carrier for sunscreens: in vitro release and in vivo skin penetration. *Journal of Controlled Release*, 81(3):225–233, 2002.

[73] Khin Yin Win and Si-Shen Feng. Effects of particle size and surface coating on cellular uptake of polymeric nanoparticles for oral delivery of anticancer drugs. *Biomaterials*, 26(15):2713–2722, 2005.

[74] Vasco Filipe, Andrea Hawe, and Wim Jiskoot. Critical evaluation of nanoparticle tracking analysis (nta) by nanosight for the measurement of nanoparticles and protein aggregates. *Pharmaceutical research*, 27(5):796–810, 2010.

[75] Bob Carr and Matthew Wright. Nanoparticle tracking analysis. *Innovations in Pharmaceutical Technology*, 26:38–40, 2008.

[76] Rebecca A Dragovic, Christopher Gardiner, Alexandra S Brooks, Dionne S Tannetta, David JP Ferguson, Patrick Hole, Bob Carr, Christopher WG Redman, Adrian L Harris, and Peter J Dobson. Sizing and phenotyping of cellular

vesicles using nanoparticle tracking analysis. *Nanomedicine: Nanotechnology, Biology and Medicine*, 7(6):780–788, 2011.

[77] E Van Der Pol, AG Hoekstra, A Sturk, C Otto, TG Van Leeuwen, and R Nieuwland. Optical and nonoptical methods for detection and characterization of microparticles and exosomes. *Journal of Thrombosis and Haemostasis*, 8(12):2596–2607, 2010.

[78] Chris Gardiner and Rebecca Dragovic. Nanoparticle tracking analysis. *Extracellular Vesicles in Health and Disease*, page 261, 2014.

[79] Robert D Boyd, Siva K Pichaimuthu, and Alexandre Cuenat. New approach to inter-technique comparisons for nanoparticle size measurements; using atomic force microscopy, nanoparticle tracking analysis and dynamic light scattering. *Colloids and Surfaces A: Physicochemical and Engineering Aspects*, 387(1):35–42, 2011.

[80] Perry Schein, Colby K. Ashcroft, Dakota ODell, Ian S. Adam, Brian DiPaolo, Manit Sabharwal, Ce Shi, Robert Hart, Christopher Earhart, and David Erickson. Near-field light scattering techniques for measuring nanoparticle-surface interaction energies and forces. *Journal of Lightwave Technology*, 33(16):3494–3502, 2015.

[81] Perry Schein, Pilgyu Kang, Dakota ODell, and David Erickson. Nanophotonic force microscopy: Characterizing particlesurface interactions using near-field photonics. *Nano Letters*, 15(2):1414–1420, 2015.

[82] Hans Saveyn, Bernard De Baets, Olivier Thas, P Hole, J Smith, and Paul Van Der Meeren. Accurate particle size distribution determination by nanoparticle tracking analysis based on 2-d brownian dynamics simulation. *Journal of colloid and interface science*, 352(2):593–600, 2010.

[83] David Erickson, Xavier Serey, Yih-Fan Chen, and Sudeep Mandal. Nanomanipulation using near field photonics. *Lab on a Chip*, 11(6):995–1009, 2011.

[84] Bradley S. Schmidt, Allen H. J. Yang, David Erickson, and Michal Lipson. Optofluidic trapping and transport on solid core waveguides within a microfluidic device. *Optics Express*, 15(22):14322–14334, 2007.

[85] Moshe Lindner, Guy Nir, Anat Vivante, Ian T Young, and Yuval Garini. Dynamic analysis of a diffusing particle in a trapping potential. *Physical Review E*, 87(2):022716, 2013.

[86] Munir El-Desouki, M Jamal Deen, Qiyin Fang, Louis Liu, Frances Tse, and David Armstrong. Cmos image sensors for high speed applications. *Sensors*, 9(1):430–444, 2009.

[87] Arindam Banerjee and Kenneth D Kihm. Experimental verification of near-wall hindered diffusion for the brownian motion of nanoparticles using evanescent wave microscopy. *Physical Review E*, 72(4):042101, 2005.

[88] Michael A Bevan and Dennis C Prieve. Hindered diffusion of colloidal particles very near to a wall: Revisited. *The Journal of Chemical Physics*, 113(3):1228–1236, 2000.

[89] Prerna Sharma, Shankar Ghosh, and S Bhattacharya. A high-precision study of hindered diffusion near a wall. *Applied Physics Letters*, 97(10):104101, 2010.

[90] Pilgyu Kang, Perry Schein, Xavier Serey, Dakota ODell, and David Erickson. Nanophotonic detection of freely interacting molecules on a single influenza virus. *Scientific Reports*, 5:12087, 2015.

[91] K Lance Kelly, Eduardo Coronado, Lin Lin Zhao, and George C Schatz. The optical properties of metal nanoparticles: the influence of size, shape, and dielectric environment. *The Journal of Physical Chemistry B*, 107(3):668–677, 2003.

[92] Ivo F Sbalzarini and Petros Koumoutsakos. Feature point tracking and trajectory analysis for video imaging in cell biology. *Journal of structural biology*, 151(2):182–195, 2005.

[93] Felipe Bernal Arango, Andrej Kwadrin, and A Femius Koenderink. Plasmonic antennas hybridized with dielectric waveguides. *ACS nano*, 6(11):10156–10167, 2012.

[94] Giovanni Magno, Aurore Ecarnot, Christophe Pin, Vy Yam, Philippe Gogol, Robert Mégy, Benoit Cluzel, and Béatrice Dagens. Integrated plasmonic nanotweezers for nanoparticle manipulation. *Opt. Lett.*, 41(16):3679–3682, Aug 2016.

[95] Peifeng Jing, Jingda Wu, Gary W Liu, Ethan G Keeler, Suzie H Pun, and Lih Y Lin. Photonic crystal optical tweezers with high efficiency for live biological samples and viability characterization. *Scientific reports*, 6, 2016.

[96] Hao Chen, Abdul M Bhuiya, Runyu Liu, Daniel M Wasserman, and Kimani C

Toussaint Jr. Design, fabrication, and characterization of near-ir gold bowtie nanoantenna arrays. *The Journal of Physical Chemistry C*, 118(35):20553–20558, 2014.

[97] M Mossayebi, AJ Wright, A Parini, MG Somekh, G Bellanca, and EC Larkins. Investigating the use of a hybrid plasmonic–photonic nanoresonator for optical trapping using finite-difference time-domain method. *Optical and Quantum Electronics*, 48(5):1–11, 2016.

[98] Nicolas G Green, Antonio Ramos, Antonio Gonzalez, Antonio Castellanos, and Hywel Morgan. Electrothermally induced fluid flow on microelectrodes. *Journal of Electrostatics*, 53(2):71–87, 2001.

[99] Justus Chukwunonso Ndukaife, Avanish Mishra, Urcan Guler, Agbai George Agwu Nnanna, Steven T Wereley, and Alexandra Boltasseva. Photothermal heating enabled by plasmonic nanostructures for electrokinetic manipulation and sorting of particles. *ACS nano*, 8(9):9035–9043, 2014.